frontiers | Frontiers in Astronomy and Space Sciences

TYPE Original Research
PUBLISHED 30 May 2023
DOI 10.3389/fspas.2023.1176158

OPEN ACCESS

EDITED BY
Fulvio Franchi,
Botswana International University of Science and Technology, Botswana

REVIEWED BY
Gene Schmidt,
Roma Tre University, Italy
Andrew Gunn,
Monash University, Australia

*CORRESPONDENCE
Sabrina Carpy,
sabrina.carpy@univ-nantes.fr

†These authors have contributed equally to this work

RECEIVED 28 February 2023
ACCEPTED 13 April 2023
PUBLISHED 30 May 2023

CITATION
Carpy S, Bordiec M and Bourgeois O (2023), Scaling laws for ablation waves formed by ice sublimation and rock dissolution: applications to the Earth, Mars and Pluto.
Front. Astron. Space Sci. 10:1176158.
doi: 10.3389/fspas.2023.1176158

Scaling laws for ablation waves formed by ice sublimation and rock dissolution: applications to the Earth, Mars and Pluto

Sabrina Carpy*†, Maï Bordiec† and Olivier Bourgeois†

Laboratoire de Planétologie et Géosciences, Centre National de la Recherche Scientifique (UMR6112), Nantes Université, Université d'Angers, Le Mans Université, Nantes, France

Ablation waves involve solid substrate such as ice or soluble rocks. Ablation by sublimation or dissolution under turbulent winds or liquid flows may lead to the development of transverse linear bedforms (ablation waves) on volatile or soluble susbtrates. In glaciology, geomorphology, karstology and planetology, these ablation waves may provide relevant morphological markers to constrain the flows that control their formation. For that purpose, we describe a unified model, that couples mass transfers and turbulent flow dynamics and takes into account the relationship between the viscosity of the fluid and the diffusivity of the ablated material, for both sublimation and dissolution waves. From the stability analysis of the model, we derive three scaling laws that relate the wavelength, the migration velocity and the growth time of the waves to the physical characteristics (pressure, temperature, friction velocity, viscous length, ablation rate) of their environment through coefficients obtained numerically. The laws are validated on terrestrial examples and laboratory experiments of sublimation and dissolution waves. Then, these laws are plotted in specific charts for dissolution waves in liquid water, for sublimation waves in N_2-rich atmospheres (e.g., Earth, Titan, Pluto) and in CO_2-rich atmospheres (e.g., Mars, Venus). They are applied to rock dissolution on the walls of a limestone cave (Saint-Marcel d'Ardèche, France), to H_2O ice sublimation on the North Polar Cap (Mars) and to CH_4 ice sublimation in Sputnik Planitia (Pluto), to demonstrate how they can be used (1) either to derive physical conditions on planetary surfaces from observed geometric characteristics of ablation waves (2) or, conversely, to predict geometric characteristics of ablation waves from measured or inferred physical conditions on planetary surfaces. The migration of sublimation waves on regions of the Martian North Polar Cap and sublimation waves candidates on Pluto are discussed.

KEYWORDS

sublimation, dissolution, instability, scaling laws, morphological markers, comparative planetology, ablation waves

1 Introduction

Because there is a large occurrence of volatile ices in the Solar System, mass transfers by sublimation and condensation are likely to shape planetary landforms (Law and Van Dijk, 1994; Kreslavsky and Head, 2002a; Byrne and Ingersoll, 2003; Hagedorn et al., 2007; Mangold, 2011). This kind of mass transfers are effective on the Martian North Polar Cap (MNPC), whose spiral troughs and sedimentation waves have been proposed to be

the result of sublimation and condensation, enhanced by the wind (Smith et al., 2013; Herny et al., 2014). While these landforms are remarkable for their size, there are many other smaller landforms like suncups giving the MNPC an overall texture of humps and hollows (Malin and Edgett, 2001; Milkovich, 2006; Banks et al., 2010; Massé et al., 2010; Nguyen et al., 2020). For all these landforms, the main processes involved in their generation are associated with phase changes enhanced by the wind (Howard, 2000) leading to a wind-driven redistribution of surface materials (ice, dust) by condensation (James, 1982; Jakosky, 1985; Fanale et al., 1992) and/or by sublimation (Ivanov and Muhleman, 2000; Ng and Zuber, 2006; Smith and Holt, 2010; Massé et al., 2012; Herny et al., 2014). On Pluto (Moores et al., 2017; Moore et al., 2018), the Bladed Terrain Deposits (BTDs) of CH_4 currently undergoing sublimation (Bertrand et al., 2019) seems to be sculpted in regular patterns by aeolian processes. On Sputnik Planitia plain, abundant sublimation pits have been observed (Moore et al., 2017) in areas where the wind seems to be weak (Bertrand et al., 2020) while linear and regularly spaced crests primarily composed of CH_4-ice (Telfer et al., 2018) has been revealed in the western region of the plain subject to stronger winds (Bertrand et al., 2020). On Earth, the pressure, temperature and humidity conditions required to allow the sublimation of icy surfaces are only found in a few specific locations. These conditions exist on some tropical glaciers at high altitude during the dry season (Winkler et al., 2009), in the Blue Ice Areas (BIAs) in Antarctica (van den Broeke and Bintanja, 1995) and in some ice caves (Curl, 1966; Obleitner and Spötl, 2011). The paucity of terrestrial observations may be why sublimation redistribution processes under turbulent wind have been poorly studied until the area of planetary space exploration.

Among the patterns generated by sublimation, we are interested in transverse linear bedforms, which are periodic ridges perpendicular to the turbulent wind. Bordiec et al. (2020) shows that sublimation waves: (1) can exist at different scales, depending on the environments and climates in which they develop; (2) can be used as morphological markers of surface-atmosphere interactions as are sand dunes (Courrech du Pont et al., 2014) thanks to scaling laws. The observation of these sublimation waves on planetary surfaces makes it possible to constrain or at least define certain characteristics of the environment: (i) the first law gives the wavelength as a function of the velocity of the flow and its viscosity; (ii) the second law links the erosion rate of the icy substrate to the migration velocity of the bedforms; (iii) the third law relates the growth time to the erosion rate and the wavelength. However, only the first law has been validated on terrestrial natural exemples (Bintanja, 1999; Obleitner and Spötl, 2011) and CO_2-ice sublimating experiment in our previous study (Bordiec et al., 2020). We are now looking for new terrestrial field analogues or laboratory experiments to assess the validity of our model in the prediction of the erosion rate. This validation step is necessary for the use of these ablation waves as morphological markers before interpreting the observations on other bodies of the Solar System.

For that purpose, we investigate other solid substrates over which bedforms developed under turbulent flows, coupled with mass transfers. Dissolving soluble rocks are good candidates: among dissolution bedforms (Allen, 1971; Meakin and Jamtveit, 2010), we identify dissolution waves refered to as fluted scallops, flutes, or solution ripples in karstology. Dissolution waves formed on a solid substrate are regularly spaced and parallel ridges, oriented perpendicular to the flow (Ford and Williams, 1989; Ginés et al., 2009), and are slightly asymmetrical in cross-section (Blumberg and Curl, 1974; Hammer et al., 2011). They appear in limestone caves (Curl, 1966; Allen, 1971; Goodchild and Ford, 1972) and their wavelength range varies from a few centimeters to several meters. They can be reproduced experimentally on soluble materials such as platinum (Thorness and Hanratty, 1979) and plaster (Blumberg and Curl, 1974). They are used in karstology to predict flow velocity and direction (Blumberg and Curl, 1974).

Thomas (1979) has compiled various examples of occurrences of bedforms on different solid substrates submitted to ablation processes by mass transfer interacting with a turbulent flow. The shapes described seem for the most part to remain independent of the substrate and the ablation and accumulation process, suggesting that the complexity associated with the chemistry of dissolution or the physics of sublimation plays only a secondary role on the final shape of these objects, possibly controlled by the hydrodynamic conditions. We seek to show that an analogy can be established between these two categories of ablation waves with similarity laws. This effort would help to complement the data set of sublimation waves with dissolution waves in order to use ablation waves as morphological markers. To that end, we combine the instability mechanism proposed by Claudin et al. (2017) for dissolution and that proposed by Bordiec et al. (2020) for sublimation. The coefficients of the scaling laws of the latter are recalculated as a function of the type of ablation (dissolution/sublimation) taking into account the viscosity of the fluid and the diffusivity of the ablated material through the Schmidt number.

A review of observations and experimental measurements are presented for sublimation waves in §2 and dissolution waves in §3. We propose new scaling laws derived from the unified model validated on previous examples in §4. In §5, the laws are plotted in a family of curves enabling to simplify the computations in different environmental conditions: (i) for planetary applications, depending on the pressure and temperature ranges of each planetary body likely to present sublimation waves at its surface and (ii) for dissolution waves in liquid water. In particular, the migration of the sublimation waves of regions of the North Polar Cap of Mars and the case of sublimation waves candidates on Pluto will be discussed. The feasibility of new experiments in terms of growth time and scale could be evaluated using the charts designed for this purpose.

2 Sublimation waves on volatile ices

Space exploration confirmed the presence of volatile ice, either water ice or ice of different compositions on many other bodies in the Solar System (**Figure 1**). Apart from the Earth where water is in a liquid state on its surface and evaporates, the most efficient phase transition in the Solar System is sublimation which allows ice to transform directly into vapor. In environments favorable to sublimation enhanced by the wind, a wide variety of solid bedforms, differing both in shape and size are observed. In this section, we identify the bodies in the Solar System for which the environmental

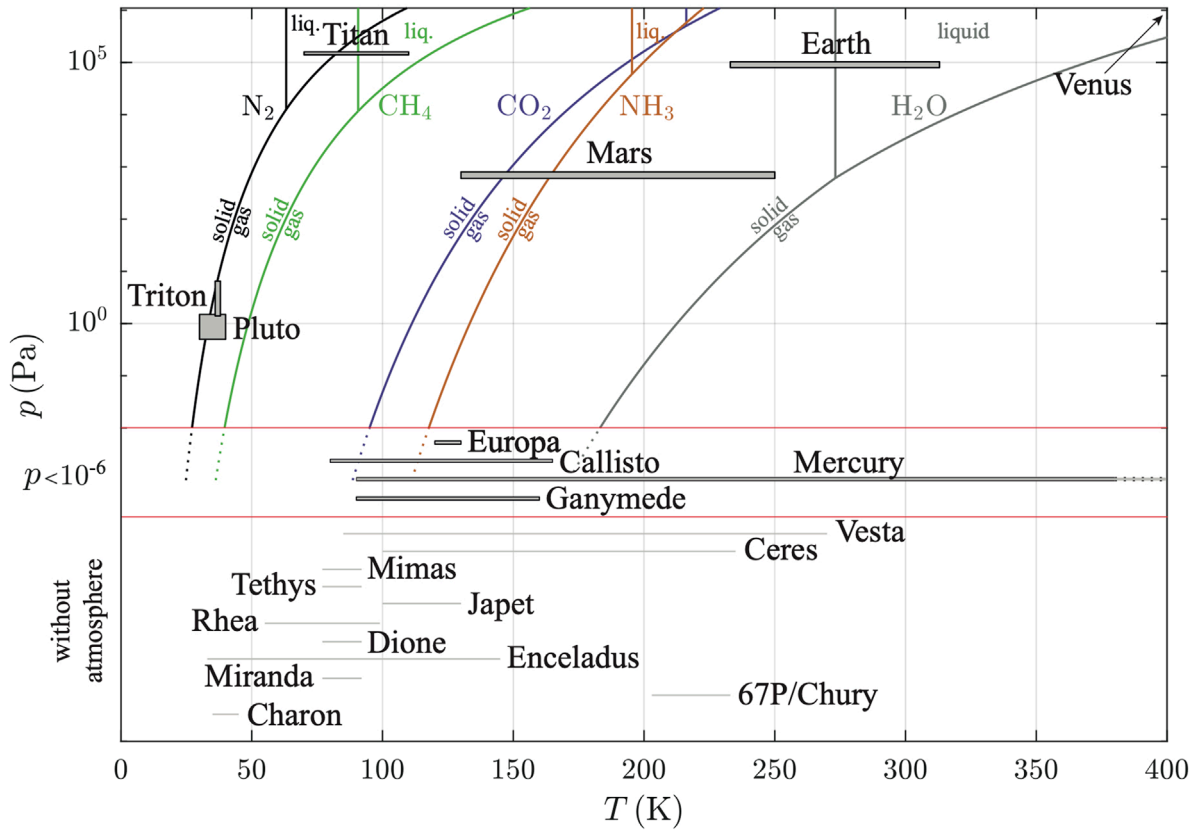

FIGURE 1
Superimposed phase diagrams of the mainly volatiles species (N_2, CH_4, CO_2, NH_3, H_2O) in the Solar System in (p,T) space, from the *Clausius-Clapeyron* relation. The mean pressure and temperature conditions of planetary bodies likely to host ice are plotted (on average, shaded areas). The upper part of the figure corresponds to bodies with an atmosphere $p > 10^{-2}$ Pa. The lower part ($p < 10^{-6}$ Pa) contains bodies with little or no atmosphere. Vapour pressure of a species has to be compared to the saturation vapour pressure to determine if sublimation/condensation occur.

conditions are favorable for the generation of sublimation waves and collect morphological and physical characteristics representative of each environment.

2.1 Volatile substrates revealed by space exploration

2.1.1 Inner Solar System

Detection of ice on Mercury is confirmed by surface reflectance measurements combined with images acquired aboard MESSENGER spacecraft. Given its small size and proximity to the Sun, the planet does not have an atmosphere and therefore has extreme temperatures at its surface (from 90 to 700 K), which do not allow ice to exist, with the exception of water ice in the permanently shaded polar regions (Eke et al., 2017). Water ice also exists on the floor of some craters and in cold micro-traps (Deutsch et al., 2017), the origin of which would come from recent impacts (Ernst et al., 2018).

On Venus, the almost exclusive composition of its thick atmosphere in CO_2 creates a greenhouse effect such that the temperature of its surface is on the order of 740 K, which makes impossible the presence of ice, whatever its nature, on its surface. Nevertheless there could be an exotic solid substrate deposit: the radar anomalies (high reflectance) linked to the presence of heavy metals (Port et al., 2020), and their deposition in the form of frost (Schaefer and Fegley, 2004) could be enhanced by the aeolian processes proposed on Venus (Kreslavsly and Bondarenko, 2017).

Water ice (seasonal snow, permafrost, pack ice, glaciers) is present in abundance on Earth (Ohmura, 2004) and the atmosphere allows to maintain stable conditions for water ice. The other gases in the atmosphere are unlikely to condense, given their phase diagrams (CO_2 and NH_3).

Instruments aboard the Lunar Reconnaissance Orbiter (LRO) spacecraft are locating and quantifying water ice on the Moon. Like Mercury, there is no atmosphere and its surface is subject to extreme temperatures and some deep polar cold traps (≃ 3.5%), which never see the Sun's rays, have exposed ice, in a mixture of ice and regolith (Li et al., 2018).

Among the many martian missions, the Mars Global Surveyor (MGS) and Mars Reconnaissance Orbiter (MRO) missions, and more recently the Trace Gas Orbiter of the ExoMars mission, are providing comprehensive information about the planet's surface and atmosphere. Currently, the thin atmosphere of Mars composed mainly of CO_2 and its distance from the Sun make it a cold planet, well below the solidification point of water, and cold enough

TABLE 1 Main composition of the atmospheres of various planetary bodies likely to undergo sublimation/deposition on their surface.

Planetary bodies	CO_2	N_2	O_2	other	Possible substrates	References
Venus	96.5%	3.5%	×	×	Lead sulf. (PbS) Bizmuth (Bi)	Lee et al. (2010) Port et al. (2020)
Earth	0.041%	78%	21%	<1%	Ice (H_2O) Ice (CO_2)	van den Broeke and Bintanja (1995) Winkler et al. (2009) Obleitner and Spötl (2011)
Mars	96%	1.89%	0.146%	<2%	Ice (H_2O) Ice (CO_2)	Hofstadter and Murray (1990) Skorov et al. (2001)
Titan	×	98.4%	×	<2%	Ice (hydrocarbons) Ice (H_2O)	Lopes et al. (2019) Mangold (2011) Hayes (2016)
Triton	×	99%	×	≤1%	Ice (N_2) Ice (CH_4) Ice (CO)	Bertrand et al. (2022) Lellouch et al. (2010) Grundy and Fink (1991)
Pluto	×	90%	×	≤10%	Ice (N_2) Ice (CH_4)	Moore et al. (2018) White et al. (2017) Protopapa et al. (2017) Bertrand et al. (2018)

to condense CO_2. Mars has two imposing polar caps mainly made up of water ice covered with CO_2 ice, seasonally for the North, and perennially for the South (Kieffer et al., 1976; James, 1982; Kelly et al., 2007; Byrne, 2009), and there are many other ice reservoirs on its surface outside the poles. Mounds of water ice has been observed on the floor of the deepest craters in the North Polar region (Conway et al., 2012) and the South Polar region (Sori et al., 2019), in which a specific and favorable microclimate allows the accumulation of ice. Moreover, underground ice, more or less covered with dust, exists on nearly a third of the Martian surface (Baker, 2001; Kreslavsky and Head, 2002b).

2.1.2 Outer Solar System

The asteroids Vesta and Ceres have been explored by the Dawn mission. The presence of water ice has been suggested at the north pole of Vesta (Stubbs and Wang, 2012; Scully et al., 2015) and assumed for Ceres from its density and shape (Carroll, 2019).

Galileo is currently the only spacecraft to have orbited Jupiter. In 2023, the ESA mission JUICE flies over and will take a closer look at the three moons Europa, Ganymede and Callisto. It will be followed by Europa Clipper, which will probe the ocean beneath Europa's ice crust. These moons are covered by a crust of water ice (Anderson et al., 1996; Khurana et al., 1998; Kivelson et al., 2000). The surface of Callisto could contain NH_3 and CO_2 ices. Io is the only moon of Jupiter's to have sulphur dioxide ice (SO_2) on its surface (Cruikshank et al., 1985).

Cassini-Huygens misson (1997–2017), has revealed among other things, the diversity of the icy surfaces of Saturn's moons. Most of them are composed mainly of water ice and rock. For example, Mimas and Tethys are mostly water ice, Iapetus and Rhea are 25% rock, and Dione, Enceladus and Titan are 50% rock. Enceladus is notable for its ice geysers (Dougherty et al., 2006) and Titan, the largest of them, has a thick, N_2 rich atmosphere. Although water ice is the majority of its internal composition, methane CH_4 undergoes a cycle in which its gaseous and liquid phases coexist, making it a water analogue for the Earth, to a certain extent (Lunine and Atreya, 2008).

Never before has a probe orbited Uranus or Neptune, Voyager 2 (1986) and New Horizons are the only probes that have made a flyby of Uranus. Among those satellites, Miranda (Uranus) presents on its surface figures adapted to an interpretation in favor of cryovolcanism and ice canyons (Schenk, 1991) and Triton (Neptune) presents a tenuous atmosphere. Triton is one of the coldest bodies in the Solar System so that N_2 condenses there as frost (Strobel and Zhu, 2017). Ice of H_2O and CO_2 could be found there.

New Horizons was intended to explore Pluto and revealed the richness of the dwarf planet in terms of composition, activity and morphological diversity. With its average temperature of 37 K, Pluto hosts N_2 ice in large quantities on its surface, as well as CO and CH_4. Apart from these highly volatile species that form its atmosphere (rich in N_2), water ice also exists, in extremely rigid form (Grundy et al., 2016). The surface of Charon is approximately the same temperature as Pluto, it contains water ice and NH_3 (Grundy et al., 2016) but without atmosphere.

The knowledge acquired on 67P/Churyumov-Gerasimienko comes from the Rosetta mission, led by ESA. Water, CO_2 and CO ices have been detected on the surface of this comet (Altwegg et al., 2015; Gulkis et al., 2015).

TABLE 2 Average values of the parameters involved in the three scaling laws of the transverse linear bedforms, for each environment where abalation waves have been observed: the upper part of the table concerns planetary environments (Forget et al., 2017; Millour et al., 2018; Bertrand et al., 2020; Bordiec et al., 2020), the lower part, the terrestrial and experimental analogues in sublimation (Bintanja, 1999; Obleitner and Spötl, 2011; Bordiec et al., 2020) and the third part the analogous experiments in dissolution (Blumberg and Curl, 1974). The values correspond either to measurements (white cells) or to predictions from the laws (grey cells). λ = wavelength, u_* = friction velocity, v_x migration velocity, q^0/ρ_s = erosion rate, t_c = characteristic time, T = temperature, P = pressure, Sc = Schmidt number.

Parameters	$\lambda[m]$	$u_*[m \cdot s^{-1}]$	$v_x[m \cdot s^{-1}]$	$q^0/\rho_s[m \cdot s^{-1}]$	$t_c[s]$	$T[K]$	$P[Pa]$	Sc
MNPC	7	0.08	4×10^{-10}	2×10^{-10}	3.9×10^{9}	210	715–740	0.42
SP Pluto	400–1,000	0.02–0.06	$6\text{-}14 \times 10^{-12}$	$3\text{-}7 \times 10^{-12}$	200–400*ky*	34–40	0.5–1.5	0.7
Svea	0.22	0.07	6×10^{-9}	3×10^{-9}	6.4×10^{6}	265	80,000–85,000	0.52
Eisriesenwelt	1.4	0.01	9×10^{-9}	4.5×10^{-9}	3×10^{7}	272	101,300	0.54
Exp. Sub. CO_2	0.06	0.2	3×10^{-6}	1.4×10^{-6}	5.4×10^{3}	293	101,300	1
Exp. Diss. 4	0.02	0.093	3.2×10^{-7}	1.5×10^{-7}	1.6×10^{4}	317.65	101,300	443
Exp. Diss. 3	0.02	0.12	3.2×10^{-7}	1.9×10^{-7}	1.37×10^{4}	300.75	101,300	875
Exp. Diss. 2	0.025	0.096	2.3×10^{-7}	1.3×10^{-7}	2.25×10^{4}	303.15	101,300	788
Exp. Diss. 1	0.05	0.06	1×10^{-7}	5.4×10^{-8}	7.3×10^{4}	296.15	101,300	1,080

2.2 Development of sublimation waves

The presence of ice, revealed by space exploration, is conditioned by many parameters such as the distance to the Sun or the presence of an atmosphere. The major species present in the Solar System (N_2, CH_4, CO_2, NH_3, H_2O) are represented in the form of phase diagrams on Figure 1. The existence of such ice depends on the availability of stable solid-state molecules for the mean pressure and temperature ranges present at the surfaces of the planetary bodies represented by shaded areas in Figure 1. We are interested in planetary bodies with an atmosphere corresponding to the upper part of the figure for which $p > 10^{-2}$ Pa. Table 1 presents the different composition of atmospheres and substrates that are possibly exposed to sublimation or condensation in those planetary environments. The physical conditions necessary for the formation of sublimation waves are present, if the following conditions are satisfied (Bordiec et al., 2020): (i) the icy surface temperatures of the species has to be lower than that of the triple point and the partial pressure of the species lower than the pressure at saturation given by the Clausius-Clapeyron diagram and calculated at the surface temperature of the icy substrate; (ii) the relative humidity of the species, less than 100%, induces a difference between the saturation vapor pressure and the partial vapor pressure sufficient to allow sublimation, at least over a period of the order of a season, taking into account the physical properties of the species at atmospheric pressure and partial pressure in the atmosphere considered; (iii) mass balances confirm the global sublimation of these icy surfaces over a given period.

2.3 Planetary examples of sublimation waves

Sublimation waves have been identified as markers of net sublimation by Bordiec et al. (2020) because their morphological and kinematics characteristics (wavelength, migration velocity, erosion rate, formation time) can be linked to their environmental conditions of formation (wind velocity, viscosity, pressure, temperature, diffusion coefficient). On Earth, transverse linear bedforms produced by sublimation are rare. Comprehensive data collected for two terrestrial natural examples and for an original sublimation experiment of CO_2 are synthesized in this section. They are completed by new observations on Mars and Pluto, that have vast icy expanses with distinctive linear dune-like patterns. All the data are summarized in Table 2 (white boxes). In all these environments, linear and transverse bedforms appear. However, they are quite different in scales and involve different compositions of the icy substrate and the atmosphere (Table 1). Despite those differences, the winds that flow on these surfaces are always turbulent and of many decades great in height in comparison to the wavelength.

2.3.1 Sublimation waves on water-ice - Earth

The first natural terrestrial example is located at *Svea* station, Antarctica (Figure 2A), on the Blue Ice Areas (BIAs), which are smooth and compact icy surfaces. The atmospheric pressure and ambient temperature conditions are in the range of 800 hPa and 850 hPa and 265 K during the austral summer, respectively (Bintanja, 1999). Mass transfer is induced by sublimation at a rate of $q^0/\rho_s \sim 10$ cm $\cdot$ yr^{-1} estimated in the absence of wind (Bintanja et al., 2001). With such a sublimation rate, the growth time of the sublimation ripples is about ~74 days. For a given turbulent wind speed of about $\simeq 2.4$ m $\cdot$ s^{-1} at an altitude $z = 6$ m and a friction velocity $u_* \simeq 0.07$ m $\cdot$ s^{-1}, the sublimation ripples measured by Bintanja et al. (2001) have an average wavelength of 22 cm with an amplitude of 10 mm and propagate in the wind direction at 2 cm $\cdot$ month^{-1}. It should be noted that the wavelength seems to be inversely proportional to the wind speed since smaller wavelengths were measured on BIAs (Weller, 1969; Mellor and Swithinbank, 1989) during stronger wind events.

The second example is the *Eisriesenwelt* ice cave, Salsbourg, Austria (Figure 2B), where dry, cold air ($T = 272$ K) from outside ($p = 1$ atm) also flows in turbulently and causes the walls to sublimate in winter. The dimensions of the sublimation waves of 1.4 m are much larger than those observed in Antarctica while

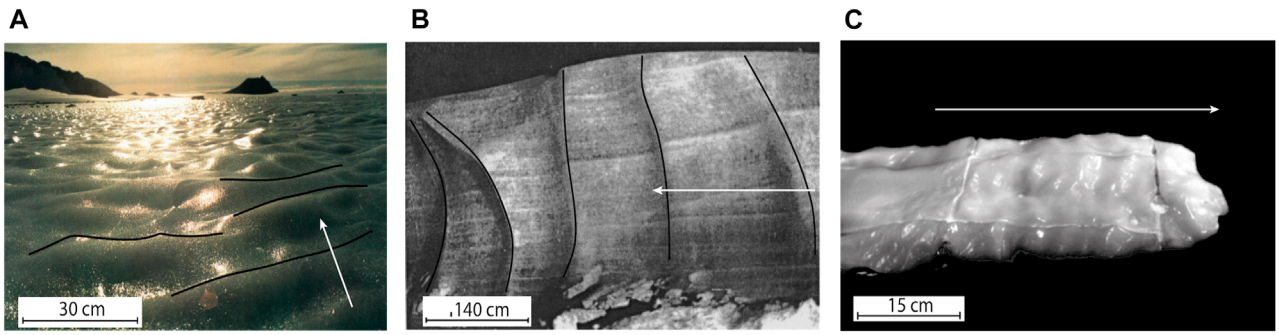

FIGURE 2
Sublimation waves: **(A)** on Blue Ice areas (Bintanja et al., 2001); **(B)** on the wall of the Eisriesenwelt ice cave (Obleitner and Spötl, 2011); **(C)** on CO2 ice in an atmospheric wind tunnel (Bordiec et al., 2020). White arrow indicates the wind direction adapted from (Bordiec et al. 2020).

the wind speed of the order of $\simeq 0.2\ \mathrm{m \cdot s^{-1}}$ is 10 times lower, so the friction velocity is smaller with $u_* \simeq 0.01\ \mathrm{m \cdot s^{-1}}$ (Obleitner and Spötl, 2011). Although mentioned, migration has never been measured and the emergence of the waves takes less than 1 year, before ice melts in summer (Curl, 1966), with a sublimation rate $q^0/\rho_s \sim 1.42\ \mathrm{cm \cdot yr^{-1}}$.

2.3.2 Sublimation waves on CO_2 ice - Wind tunnel experiment

An analogical experiment to sublimation waves of water ice in Antarctica was proposed by Bordiec et al. (2020) to test whether the coupled action of wind and sublimation can generate bedforms in a windy controlled environment, in the atmospheric wind tunnel in Nantes, France (LHEEA, UMR6598), using CO_2 ice as it sublimates at ambient pressure and temperature conditions ($p = 1$ atm, $T = 293$ K). In net ablation with a sublimation rate measured in the absence of wind of $1.4 \times 10^{-6}\ \mathrm{m \cdot s^{-1}}$, these ice blocks subjected to a turbulent flow at $U = 6\ \mathrm{m \cdot s^{-1}}$ with $u_* \simeq 0.2\ \mathrm{m \cdot s^{-1}}$ presented, after ~ 4 h, centimeter-scale undulations on their surface about 6 cm in wavelength (**Figure 2C**). Migration of the ripples could not unfortunately be measured but predicted to be of the order of $1.\ \mathrm{cm \cdot h^{-1}}$ by Bordiec et al. (2020).

2.3.3 Sublimation waves on water-ice - Martian North Polar Cap

To explore the possibility that these type of new morphological markers exists among sublimation patterns described on the MNPC, images of the region located at the boundary between *Boreales Scopuli* and *Olympia Cavi* ($82°N, 120°E$) were studied by Bordiec et al. (2020), when water ice is exposed to sublimation for a period between $Ls = 90°$ and $Ls = 135°$, with a maximum between $Ls = 100°$ and $Ls = 120°$ (Pankine et al., 2010). During this period, surface temperature is ($T \simeq 210$ K) and vapour pressure ($P \simeq 730$ Pa) (Pankine et al., 2010) with a sublimation rate estimated at $q^0/\rho_s \sim 2. \times 10^{-10}\ \mathrm{m \cdot s^{-1}}$ (Chittenden et al., 2008). These patterns are identified in **Figure 3**, they are linear and parallel ridges, generally oriented along the North-South direction. Nguyen et al. (2020) suggested that these shapes are different from classical Martian aeolian dunes and Bordiec et al. (2020) propose that the process responsible for their formation is sublimation coupled with a turbulent winds. The turbulent boundary layer thickness about $\simeq 10$ km (Pankine and Tamppari, 2015) is greater than the observed wavelength with $\lambda \simeq 7$ m. The katabatic winds flow in summer (Howard, 2000; Kauhanen et al., 2008; Petrosyan et al., 2011) over the region. We can estimated the wind speed around $\simeq 2.5\ \mathrm{m \cdot s^{-1}}$ ($u_* \simeq 0.08\ \mathrm{m \cdot s^{-1}}$) using GCM data base (Forget et al., 1999; Millour et al., 2018) at 100 m above the surface of this region. The orientation of the prevailing winds in this region, deduced from mesoscale numerical simulations of Smith and Spiga (2018), is east-west. This is confirmed by the orientation of the wind streaks around a crater located in the same region (Bordiec et al., 2020). The bedforms are therefore transverse, perpendicular to the prevailing winds.

To complete the morphological analysis with a kinetic study of these objects, we compare all the *HiRISE* images at the horizontal resolution of 25 cm/pixel, available in the region since the camera was operational in 2008. Ripple crests over this region have been located between 2008 (**Figure 3A**) and 2019 (**Figure 3B**) during the northern Martian summer ($Ls = 115°$). The selected crests are considered to be as close as possible to the crater that serves as a fixed reference for georeferencing the images. **Figure 3C** shows that the crest lines overlap and does not allow the observation of any evolution in time of these undulations between 2008 and 2019, or by such a small amount that this difference could not be detected.

2.3.4 Candidate sublimation waves on CH_4 ice – Sputnik Planitia, Pluto

At present, the mean surface temperature of Pluto is around $T = 37$ K and an atmospheric pressure between $p = 0.5$ and 1.5 atm. Pluto shares similarities with Mars: a tenuous atmosphere with a complex climatic system driven by the redistribution cycles of volatile ices. Pluto's atmosphere is very rich in N_2 and the conditions at its surface are such that it is now known that the successive cycles of sublimation and condensation of N_2 but also CH_4 are not only active processes but also partly responsible for the diversity of landscapes (**Figure 4**) on the surface (Bertrand et al., 2018; Bertrand et al., 2019). Among the great diversity of landforms on Pluto, Sputnik Planitia (**Figure 4A**), a large basin covering more than 30° in latitude composed of a complex mixture of

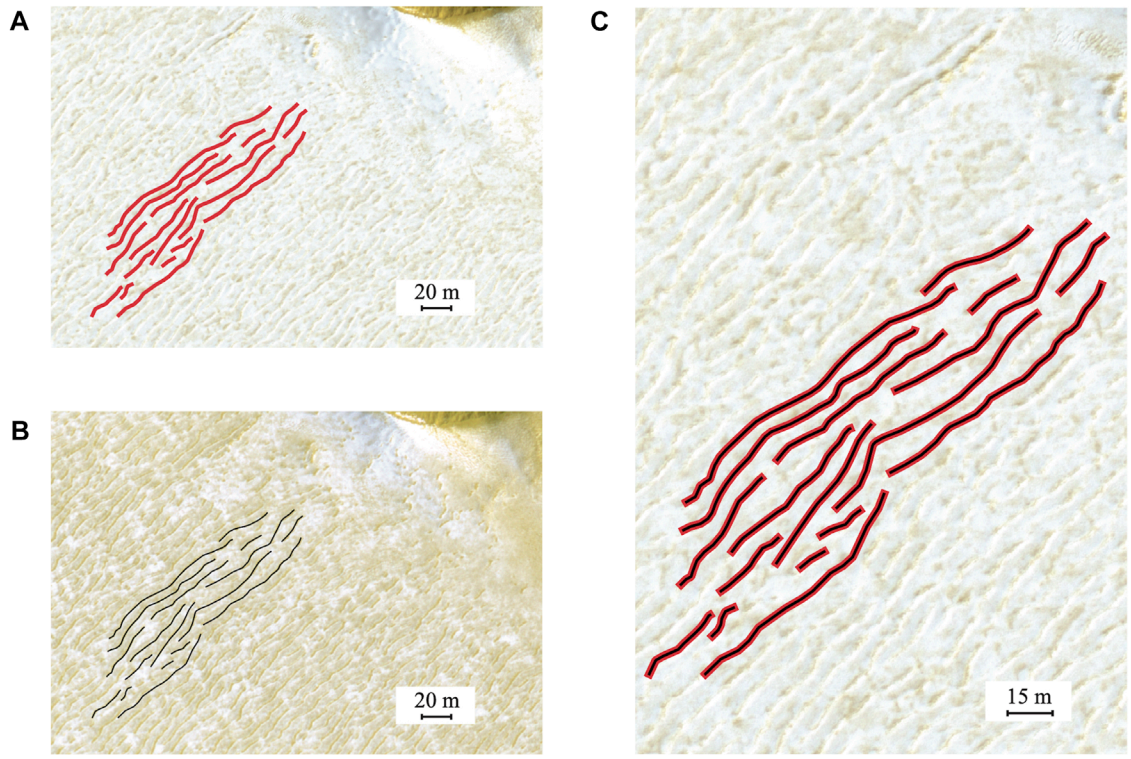

FIGURE 3
Comparison of the location of the crests of the sublimation waves of the MNPC between 2008 and 2009 during the northern Martian summer (*Ls* =115°). **(A)** Image ID HiRISE: PSP_009689_2645; credit: NASA/JPL/University of Arizona obtained on 20 August 2008. Spatial resolution is 25 cm/pixel. Crests are highlighted in thick red lines. **(B)** Image ID HiRISE: ESP_062580_2645; credit: NASA/JPL/University of Arizona obtained on 2 December 2019. Spatial resolution is 25 cm/pixel. Crests are highlighted in thin black lines. **(C)** Zoom of the surface (PSP_009689_2645, 2008) with superimposed crest lines from figures **(A, B)**. The undulations are considered as close as possible to the crater, which serves as a fixed reference for georeferencing the images. The superimposed crest lines indicate that they have not moved between 2008 and 2019, or by so little that this difference could not be detected.

N_2 ice, and to a lesser extent CO and CH_4 ices (Schmitt et al., 2017), is the most emblematic. Sublimation is currently dominant above 15°N, at a rate estimated to $q^0/\rho_s \sim 3-7\times10^{-12}$ m·s^{-1}, while condensation dominates below (Bertrand et al., 2018). This plain contains many characteristic shapes (**Figure 4B**), such as polygonal cells over ≃ 10 km wide interpreted as resulting from thermal convection of the ice (McKinnon et al., 2016; Trowbridge et al., 2016; Morison et al., 2021) and bordered by pits over 100 m deep. These remarkable shapes provide an additional argument to that of the absence of craters on the whole Sputnik Planitia, in favor of the hypothesis of a geologically young and active surface (<500 ka) (McKinnon et al., 2016; Trowbridge et al., 2016).

A surface texture consisting of pits, typical of the circular shapes created by sublimation and regularly distributed in space, is the dominant texture in the southern part of the plain (Moore et al., 2017). To the northwest, the basin is bounded by the *al-Idrissi* mountains composed of water ice, next to which, over an area of ≃ 75 km from these mountains (latitude ≃ 30°N, longitude ≃ 160°E, **Figure 4C**), linear ridges regularly spaced (0.4–1 km) were observed by Telfer et al. (2018) on a substrate composed of CH_4 and N_2. With distance from the mountains, these ridges become spaced further apart and are arranged in patches. Wind streaks behind certain obstacles also attest to the direction of the wind, consistent with the local topography, and that seems to be perpendicular to the orientation of these ridges (Telfer et al., 2018). Indeed, the winds on Sputnik Planitia seem to be locally induced by the condensation and sublimation of N_2 (Forget et al., 2017) and by the so-called katabatic gravity flow on topographic slopes that are linked to the temperature difference between the colder surface and the warmer atmosphere. Winds are generally turbulent near the surface (boundary layer of thickness ≃ 15 km) and modeling of their circulation indicates that their speed could reach several meters per second (at 20 m above the surface) although it would generally be less than 1 m per second (Forget et al., 2017). Since the strongest winds are expected to occur where the topographic gradients are greatest the northwestern part of Sputnik Planitia on which the ridges appear would correspond to a very windy region (Telfer et al., 2018) and areas with more widely spaced ridges to more moderate winds.

One of the interpretations proposed so far to explain the formation of the linear ridges in northwestern of Sputnik Planitia is that they are dunes formed by grains of CH_4 ice, whose movement would be initiated by sublimation because the friction velocity of the local winds is not strong enough to reach the threshold friction velocity to set the grains in motion, and would then be maintained by

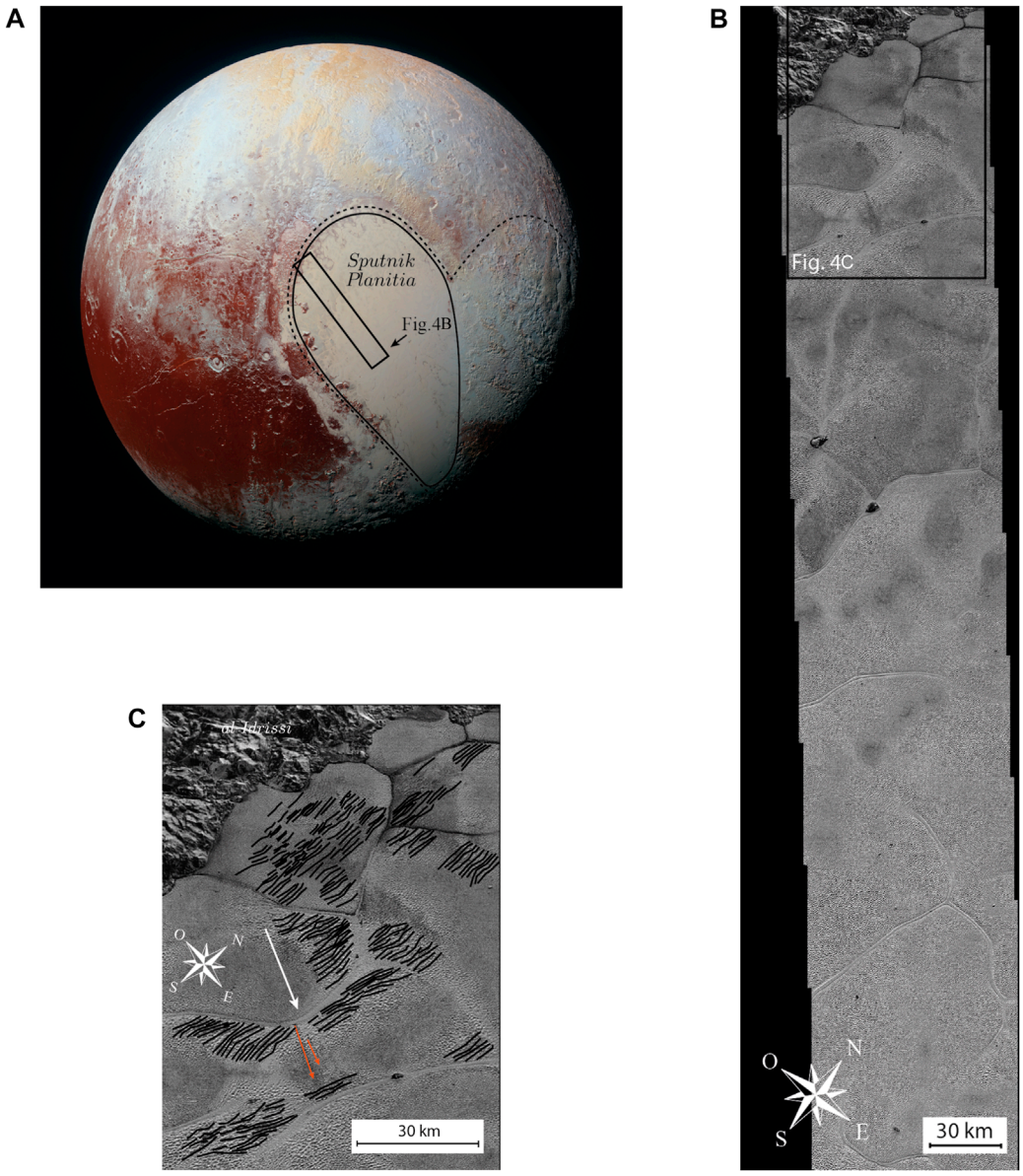

FIGURE 4
Pluto and its regions of interest, 14 July 2015 (credit: NASA/JHUAPL/SwRI). **(A)** Global view of Pluto in colour, taken by the Ralph/Multispectral Visual Imaging Camera (MVIC) on New Horizons. The "heart" of Pluto is dashed and the region of *Sputnik Planitia* is highlighted. **(B)** Image of part of Sputnik Planitia, taken by the Long Range Reconnaissance Imager (LORRI), at a resolution of 77 to 85 m/pixel. **(C)** Zoom on the linear and regularly spaced crests of the western region of Sputnik Planitia bordered by the *al-Idrissi* mountains and superimposed on polygonal cells. The crest lines are underlined in black while the white arrow indicates the wind direction deduced from the streaks (in orange) and the surrounding topography (modified from Telfer et al. (2018)).

local winds (Telfer et al., 2018). Nevertheless, Gunn and Jerolmack (2022) show that even the threshold to maintain grain transport (friction velocity is about $u_* = 1.\ \mathrm{m \cdot s^{-1}}$) is too high for the proposed wind speeds over Sputnik Planitia. By analogy with observations of sublimation ripples in Antarctica, in ice caves and on the MNPC, it would seem that the main ingredients required in each of these environments are also present on Sputnik Planitia, suggesting that an alternative hypothesis could be that these ridges are the result of sublimation (without grain transport) coupled with turbulent winds.

3 Dissolution waves on soluble rocks

Ablation waves occur on solid substrates that are subject to mass transfer at their surface. The flow of liquid like water can dissolve some rocks. If dissolution waves, i.e., flutes/solution ripples are mentioned and visibly widespread (Ford and Williams, 1989; Ginés et al., 2009), complete natural data sets on the subject are paradoxically lacking. The description of their form, occurrence and the environments in which they develop, through natural examples and laboratory experiments, borrowed from a field analysis and the

existing literature is the subject of this section. The only complete experiment on the specific subject of flutes/solution ripples on a dissolving solid substrate of which average parameters measured are given in **Table 2** (white boxes), is the dissolution laboratory experiments run by Blumberg and Curl (1974).

3.1 Soluble rocks on Earth

Carbonate rock and evaporite outcrops are widespread on Earth and very often form complex systems of landscapes dotted with caves and underground networks in which water circulates. The type of system that is created on these soluble rocks are called karsts. Karst landforms occupy no less than ~20% of the Earth's continental surface not covered by ice (Ford and Williams, 1989), and thus represent a significant reservoir of soluble rocks. Evaporites are globally distributed over all continental surfaces but are more common in the Northern Hemisphere (Ford and Williams, 1989). Although they are less exposed than carbonates, there are large evaporite karsts in China, Ukraine, the United States but also smaller ones in many other countries and in various environments (Milanovic et al., 2019). They are formed by homogeneous or heterogeneous precipitation in waters with high concentrations of dissolved ions, induced by partial evaporation. Thus, seawater is quantitatively their most important source, through lagoons or subtidal, intertidal and supratidal areas of salt plains (*sebkha*). In arid and semi-arid environments, the sources are dry lakes, thus forming the *salar*, *salina* or *playa* (Ford and Williams, 1989).

3.2 Development of dissolution waves

3.2.1 Mineral composition

Soluble rocks and particularly carbonate rocks are composed of minerals such as calcite and dolomite, and evaporitic rocks are composed of sulphates or chlorides. Evaporite karsts are mainly composed of gypsum ($CaSO_4$, H_2O), the most common sulphate mineral among evaporites. After carbonates, it is indeed the mineral that precipitates the fastest, before its dehydrated forms (anhydrite $CaSO_4$ and halite NaCl). Since it only appears after gypsum and because the waters of lagoons and intertidal zones are generally renewed before it precipitates, halite is less widespread, except in the case of arid regions where the waters are endoreic, i.e. hydrologically closed lakes that do not drain to the sea. Salt karsts are therefore limited to patches in these deserts and, despite the fact that they are ephemeral and relatively young (for those that currently exist) in view of the high solubility of halite and its fragility, remain little studied (Frumkin, 1994; Frumkin, 2013).

3.2.2 Kinetics of dissolution

The process of accumulation and removal of water-soluble rocks is chemical: dissolution/precipitation reactions are mainly involved. When a rock dissolves in water, some or all of its individual minerals disintegrate into individual ions or molecules that are then diffused into the solution. Calcite, gypsum and halite dissolve by dissociation according to the reactions given in **Table 3**. They dissolve in water, the viscosity of which depends mainly on the temperature (Kaufmann et al., 2014).

Classically in chemical kinetics, the dissolution of a solid in a solution is separated into several distinct physical or chemical steps (Morse and Arvidson, 2002): (i) the transport of the reactive agents from the liquid to the solid surface, (ii) the adsorption of reactive substances on the surface, (iii) the chemical reaction between the adsorbed reagents and the solid surface, which may also contain several steps, (iv) the desorption of products into solution, (v) the transport of products and their diffusion in the solution.

The overall kinetics of the transfer is therefore limited by which of these steps is the slowest. For calcite, which has more dissolution-precipitation reactions than gypsum or halite, the kinetics is influenced by numerous parameters, such as the acidity (pH) the partial pressure of CO_2 (p_{CO_2}), the temperature (T), the state of saturation (SI) but also, transport of ions and molecules by a flow (as for sublimation hydrodynamic conditions) and the shape of the surface. The determination of the limiting process therefore depends on the conditions related to the control parameters.

The kinetics of dissolution is thus controlled sometimes by transport, sometimes by chemical reaction, and sometimes both at the same time, that leads to a mixed behaviour. Thereafter, we are interested in processes dominated by the transport of particles (vapour, ions in solution) by advection-diffusion in a flow. In this case, the dissolution rate defined by q^0/ρ_s is very small compared to the friction velocity u_* of the flow (**Table 2**).

3.3 Terrestrial examples of dissolution waves

3.3.1 Dissolution waves on limestone - Saint-Marcel d'Ardèche cave, France

The linear transverse undulations produced by dissolution exist mainly on the walls of caves in soluble rocks, as in the cave of *Saint-Marcel d'Ardèche*, France, in calcite. It is characterised by large volumes, a rich concretion and shows many forms of dissolution on its walls. The galleries of the network contain a fine detrital filling composed of beige and red mica sands and clays. Between the demarcations linked to the successive sections of the gallery, transverse and linear ridges have developed, among other forms (**Figure 5**).

In order to characterize these forms morphologically, a few selected walls on network I were scanned using a portable LIDAR, in the *Gallerie des peintres* or *Gallerie des maçons*. The topographic data acquired with the LIDAR allowed the production of 3D surfaces by interpolation of point clouds (**Figure 5A**) and 2D profiles of the shapes (**Figure 5B**). The general shape of the ripples is not sinusoidal but some periodicity of the peaks is observed. With a wavelength $\simeq$ 1 m and an amplitude $\simeq$ 0.1 m, their aspect ratio is of the order of $R_a \simeq 0.1$. Their transverse profile is asymmetrical and has a steeper slope on the downstream side than on the upstream side. No information on the formation of these undulations can be acquired so controlled experiments are required to complement **Table 2**.

TABLE 3 Dissolution reactions, orders of magnitude of diffusion coefficients D and dissolution fluxes q^0 of the main minerals constituting soluble rocks, at 25°C and 5 < *pH* <9, from Ford and Williams (1989); Morse and Arvidson (2002); Daupley et al. (2015).

Mineral	Dissolution reaction	$D[m^2 \cdot s^{-1}]$	$q^0[kg \cdot m^{-2} \cdot s^{-1}]$	References
Calcite	$CaCO_3 + CO_2 + H_2O \leftrightarrow Ca^{2+} + 2HCO_3^-$	9×10^{-10}	$\sim 10^{-7}$	Cubillas et al. (2005)
Gypse	$CaSO_4 \cdot 2H_2O \rightarrow Ca^{2+} + SO_4^{2-} + 2H_2O$	10^{-10}	$\sim 10^{-5}$	Ginés et al. (2009), Daupley et al. (2015), Colombani and Bert (2007)
Halite	$NaCl + H_2O \rightarrow Na^+ + Cl^- + H^+ + OH^-$	10^{-10}	$\sim 10^{-3}$	Ginés et al. (2009), Daupley et al. (2015)

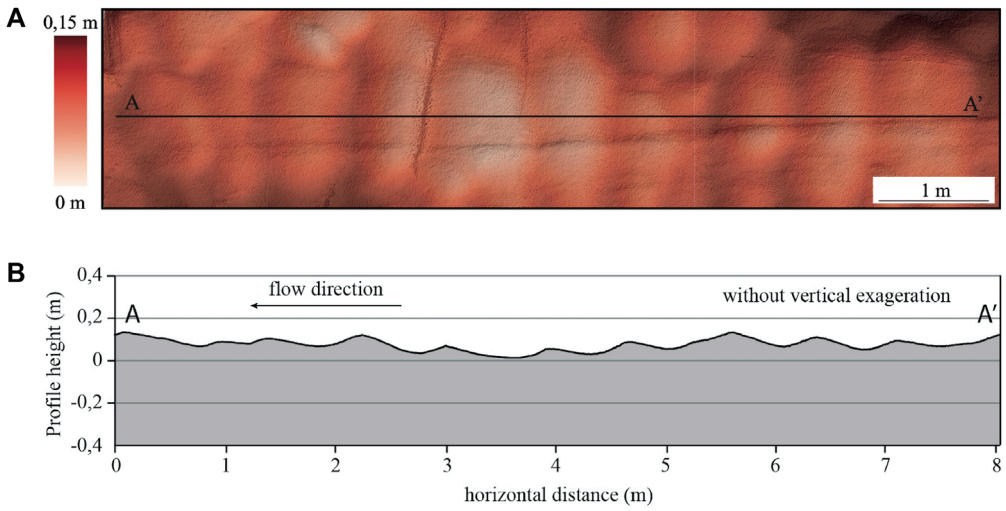

FIGURE 5
Typical shape of the dissolution waves visible on the wavy walls of the *Galerie des Peintres* of the Cave in *St-Marcel d'Ardèche*, France. **(A)** Raster image of the wall, obtained by interpolation of LIDAR point clouds. The black line symbolises the cross-sectional AA' line that allows the typical profile to be visualised. **(B)** Typical profile according to section AA'.

3.3.2 Dissolution waves on gypsum - Laboratory experiments

The experiment of Blumberg and Curl (1974) consists in reproducing dissolution waves on a soluble substrate in the laboratory (**Figure 6**). They study their stability, through the wavelength, the migration, the general temporal evolution, the dissolution rate and more generally, the mass transfer that takes place. Their choice of substrate is gypsum (calcium sulphate hemihydrate), whose dissolution is ensured throughout the experiment by maintaining a reagent concentration at 10% from saturation, by replacing part of the solution with the same volume of fresh water continuously. The experiment is carried out in a hydrodynamic tunnel of cross-section 15.25 cm × 15.25 cm, imposing a hydrodynamic boundary layer of ≃ 7.6 cm. The temperature is continuously monitored and the flow velocity U is measured at all times by pitot tubes. The block of gypsium, of size 76.2 cm × 15.25 cm × 12.7 cm, is placed in the centre of the tunnel.

The authors indicate that the length of the hydrodynamic tunnel is not sufficient to create dissolution waves spontaneously, so grooves transverse to the flow were made on the surface of the block at regular intervals, on which the ripples are supposed to develop. The authors admit that this approach does not allow the exact determination of the equilibrium situation of the dissolution waves, i.e. the growth time at which they should have emerged spontaneously from an initially flat surface. The disturbance of the topography predefined by these grooves seems however not to influence the wavelength and the final profile of the dissolution waves since the various tests carried out by Blumberg and Curl (1974) with several extreme intervals, demonstrate that the ripples develop on the grooves and then evolve by gradually increasing or decreasing the wavelength progressively until a certain common equilibrium is reached.

Due to combined effects of dissolution and different turbulent flow velocities, these dissolution waves have a centimeter spacing (2–5 cm and a millimeter amplitude and migrate at different velocity $1–3.2 \times 10^{-7}$ m · s^{-1} in the direction of flow. During their series of experiments, the device allowed the measurement of the parameters ϕ, the propagation angle and v_z, as well as the local values of the slopes θ, that allowed them to generalize the shape of the profiles obtained (**Figure 6A**). Their measurements (see Blumberg and Curl (1974) for details of the methods) provide an estimate of the local vertical dissolution rate $v_z = q^0/\rho_s$, where q^0 is the flux density at the wall. Using the measured values of the propagation angle ϕ in the Blumberg and Curl (1974)'s experiments, the horizontal migration velocity can be deduced geometrically (see **Figure 6B**)

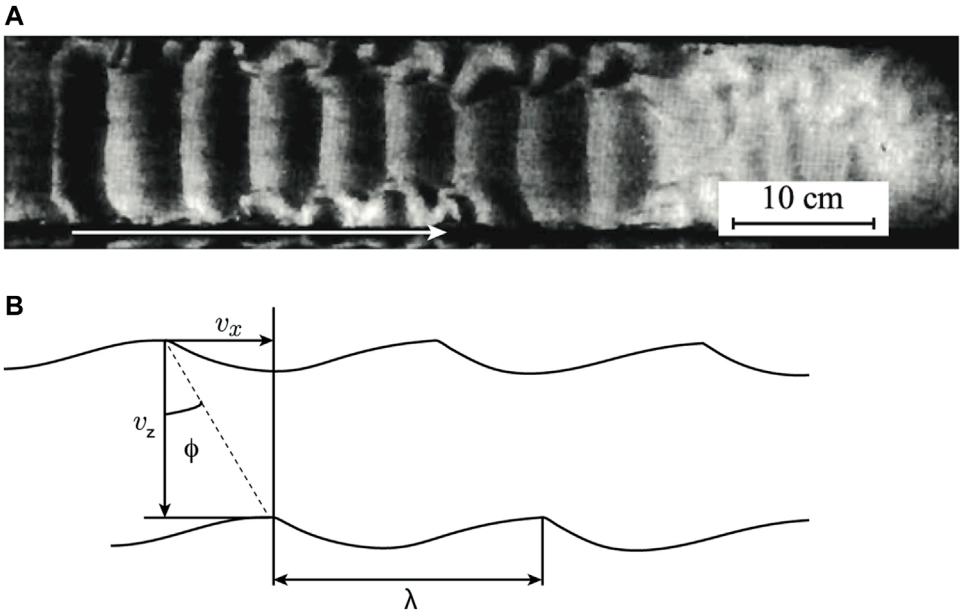

FIGURE 6
Dissolution experiment adapted from Blumberg and Curl (1974). **(A)** Dissolution waves (Exp. 1). The wavelength is 5 cm. The white arrow indicates the direction of flow. **(B)** Profile and geometrical parametrisation of the dissolution waves. The lower profile corresponds to its evolution over time, after dissolution. ϕ is the propagation angle, and v_x the migration velocity.

as a function of the propagation angle and the sublimation rate:

$$v_x = tan(\phi)\ \ q^0/\rho_s \tag{1}$$

The main results of these experiments are listed in **Table 2** (white cells). It should be noted that the growth times of bedform formation have not been measured but could be estimated. Indeed, all the data collected in **Table 2** are complemented by additional calculations (grey cell) from the scaling laws presented in next section 4.

4 Scaling laws for ablation waves: a unified model

Ablation waves involve solid substrates, such as ice (§2), but are also found on soluble rocks (§3). Perturbations of a flat substrate, without characteristic or periodic length, disturb the flow that modifies the mass transfer that in turn modifies the topography. This positive feedback can initiate an unstable system, i.e. one that does not return to its initial state following a disturbance or disturbances. The role of morphogenesis is to consider how to relate the characteristics of topography to those of flow and mass transfer. While several approaches exist, instability theory and in particular linear stability analysis, which relates the growth of disturbances to the growth of instabilities, seems to be the most relevant (Gallaire and Brun, 2017).

4.1 Ablation by sublimation or dissolution: an analogous instability mechanism

Mass transfers shape solid substrates by ablation under a turbulent flow. Sublimation is a physical transformation of phase change between the solid and vapour phase without passing through the liquid phase, whereas dissolution is based on chemical reactions between ions in solution and molecules. These transfers are therefore different in nature but both involve a variation in enthalpy and have a similar formulation of their equilibrium (saturation vapour pressure and equilibrium constant, resp.). The direction of the transfer is in both cases conditioned by the value of a relative quantity that determines whether the system is saturated or not (relative humidity and saturation index, resp.). The kinetics of the transfers can be considered at the microscopic scale (kinetic theory, chemical kinetics, resp.) at the interface or extrapolated to the continuous medium when the transport of particles (vapour, ions in solution, resp.) is based on advection-diffusion in a flow. In both cases, the quantification of the material flow is proportional to the difference between the concentration and the equilibrium concentration, weighted by a kinetic coefficient depending on the type of transfer. This approximation is valid at the macroscopic scale where the transport of vapour or ions in solution, resp., is by advection and diffusion in a turbulent near-wall flow.

The sublimation and dissolution waves could be analogous as long as the instability mechanism responsible for their development is robust (Gallaire and Brun, 2017). If so, their shape and their kinetics depend on a combination of physical parameters, through dimensionless numbers driving the problem, with at least one of these numbers being conserved whatever the type of transfer so

that there is similarity. The friction velocity u_* and the viscosity ν of the underlying turbulent flow seem to control the characteristic length scale λ of the waves through a coefficient whose value seems to be linked to the type of transfer that is characterized by the ratio between the viscosity of the flow ν and the diffusivity coefficient D of the substrate in the flow. As can be seen in **Table 2** (i) the Schmidt number ν/D depends on the type of transfer, from ~1 in sublimation to 10^3 in dissolution, this number is therefore a variable of the problem; (ii) the mean value of $k\nu/u_* \sim 10^{-3}$ depends slightly on the type of transfer. This latter dimensionless number that is in fact the inverse of a Reynolds number Re^{-1} related to the wave number $k = \frac{2\pi}{\lambda}$, seems to confer an analogical character of the two mass transfers at first inspection. Furthermore, the angle ϕ is constant in the laboratory dissolution experiment, despite the variation of the Schmidt number. Should we expect this value to be constant also in sublimation? The propagation angle being linked to the migration speed and the erosion rate (Eq. **1**), we propose to study these parameters as a function of the dimensionless numbers of the problem (Re^{-1}, Sc) through a stability analysis.

4.2 Stability analysis of the coupled ablative mass transfer and near-wall turbulent flow

The objective of the temporal stability analysis is to study the stability of the solid-substrate/flow interface with time. The interface profile is generally written:

$$\zeta(x,t) = \zeta_0 e^{\sigma t}\Re\left(e^{i(kx+\omega t)}\right), \tag{2}$$

where ζ_0 is the amplitude, $k = \frac{2\pi}{\lambda}$ the wavenumber, λ the wavelength and σ the time growth rate associated with the wavenumber k and the pulsation ω. The disturbance of the flow linked to this profile is also sinusoidal and proportional to $k\zeta_0$.

The ablation wave emerge if $\sigma > 0$ (they are unstable), while they disappear if $\sigma < 0$ (they are stable). Their migration speed that is equal to $-\omega/k$ is in the direction of flow if $\omega < 0$ and in the opposite direction of flow if $\omega > 0$. The determination of the dispersion relation of the system makes it possible to highlight the values of k for which $\sigma > 0$ and to identify the most unstable mode for which σ is maximal.

The linear approach works even if the aspect ratio $R_a = \frac{2\zeta_0}{\lambda}$ is more than 0.03. Kuzan et al. (1989)'s experiment shows even if instantaneous flow reverses direction, the time-averaged flow is non-separated and this depends on $\frac{k\nu}{u_*}$ so that the limit could be bigger for dissolution waves $R_a \simeq 0.125$ than for sublimation waves $R_a \simeq 0.05$. If this aspect ratio increases too much, the smooth limit is no longer applicable and the bed roughness linked to the presence of the ablation waves on the substrate must be taken into account (Claudin et al., 2017; Durán et al., 2019). The linear approach is still valuable but roughness introduces a stabilising effect so that the ablation waves can then disappear ($\sigma < 0$) if the Reynolds number based on the bed roughness r length scale is such that $R_r = \frac{ru_*}{\nu} \geq 100$. Above this value, the hydrodynamical response of the flow to the bed topography becomes independent of roughness, and then just depends on the wavelength λ of the bed and the type of the mass transfer.

By studying the stability of the coupled flow dynamics and mass transfer system, it has been shown that the combined effect of winds and sublimation (Bordiec et al., 2020) or water flow and dissolution (Claudin et al., 2017) lead to the formation of ablation waves, i.e. $\sigma > 0$, for a given wavelengths range in a transition regime between laminar and turbulent flow for a wall-Reynolds number based on the bedform's wavelength $\mathrm{Re} = \lambda u_*/\nu \sim \frac{u_*}{k\nu} \sim 10^3$. If the global turbulence of the flow is taken into account according to the RANS statistical method, the wall-Reynolds number based on the wavelength requires the use of a near-wall turbulence RANS model (Knotek and Jícha, 2014) able to better reproduce the evolution of the friction coefficient with the Reynolds number (Manceau et al., 2002; Jakirlić et al., 2009). In our model, we use a closure based on the turbulent viscosity with a mixing length according to the Loyd and Hanratty formulation (Hanratty, 1981), designed for this purpose. Then we perform a linear stability analysis of the model following Claudin et al. (2017) and Bordiec et al. (2020) considering the smooth limit $R_r \to 0$ with a variation of the Schmidt number from ~1 to 10^3. The novelty of this study is that we explore all the parameters of the dispersion relation, including the propagation angle, by varying the Schmidt number to deal with both the sublimation and dissolution problems.

4.2.1 Dimensionless numbers of the problem

Afterwards, the following configuration is considered: a flow of many decades great in height with respect to the wavelength of the bedforms, in a hydrodynamically smooth regime ($R_r \to 0$), by limiting to the linear effects of the instability. From the parameters and dimensional considerations, it is possible to highlight four dimensionless numbers characteristic of the problem.

(i) The Schmidt number Sc compares the effects of momentum and mass diffusivity. It is defined by $Sc = \frac{\nu}{D}$,

(ii) The dimensionless wavenumber is the one that controls the near wall regime:

$$k^+ = k\frac{\nu}{u_*} = Re^{-1}, \tag{3}$$

(iii) The dimensionless growth time is defined by:

$$\sigma^+ = \sigma\frac{\rho_s}{q^0}\frac{\nu}{u_*}, \tag{4}$$

(iv) The dimensionless number pulsation ω^+ is defined by:

$$\omega^+ = \omega\frac{\rho_s}{q^0}\frac{\nu}{u_*}, \tag{5}$$

The ratio $-\omega^+/k^+ = \tan(\phi)$ defines the propagation angle.

4.2.2 Dependance on the Schmidt number

Since the diffusion coefficient is much lower in liquids than in gases, the order of magnitude of Sc is typically 10^3 in liquids, while it is only unity in gases (Incropera et al., 2007). Although different, the values of the Schmidt number in the different environments described § 2 for sublimation remain of the same order of magnitude ($Sc \simeq 1$) whereas for dissolution, the experiments described in § 3, the Schmidt number is variable, between 10^2 and 10^3 (**Table 2**). The dispersion relation displayed in **Figure 7** explores the instability. In

the $(Sc, kv/u_*)$ plane, the unstable domain is defined on **Figure 7A** by a shaded area corresponding to $\sigma^+ > 0$ for which the scaled wavenumbers k^+ belongs to the near-wall regime of laminar-turbulent transition. The maximum growth rate σ_c^+ (solid lines) corresponds to the most amplified wavelength k_c^+ (dashed lines). Thus, it appears that the Schmidt number has little influence on the instability domain and on the most unstable mode. However, it should be noted that the $\frac{kv}{u_*}$ range of the band instability considering variations in Schmidt and wall-Reynolds numbers decreases with increasing Sc.

Figure 7B shows the evolution of the dimensionless numbers of the dispersion relation, characteristic of the instability, as a function of the increasing Schmidt number. The numerical results show that σ_c^+, k_c^+ and ω_c^+ all depend on the Schmidt number, dividing k_c^+ by $\simeq 6$ and the growth rate σ_c^+ by $\simeq 3$ between $Sc = 1$ and $Sc = 10^3$. For k_c^+ the obtained values are in accordance with **Table 2** over the range $1 < Sc < 10^3$ for which this quantity evolves as $Sc^{-1/5}$. The evolution of ω_c^+ is the same of k_c^+ and depends on $Sc^{-1/5}$ whereas σ_c^+ decreases as a function of $Sc^{-1/6}$. It is therefore necessary to take into account the influence of this Schmidt number in the scaling laws initially proposed by Bordiec et al. (2020) for sublimation in order to establish the similarity between sublimation and dissolution waves.

The experimental propagation angle ϕ, defined in Section 3.3.2 (**Figure 6B**), appears to be relatively constant ($\phi \simeq 63.5°$) in the dissolution experiments (Blumberg and Curl, 1974) for different Schmidt numbers. This can be explained by the fact that ω_c^+ and k_c^+ obtained numerically (**Figure 7B**) have the same evolution as a function of Sc. Consequently the ratio of these two quantities involved in the definition of the propagation angle (Eq. **1**) becomes independent of Sc. The study of the variability of $\tan(\phi)$ as a function of the dimensionless wavenumber for different Schmidt numbers (**Figure 7C**) show that the value $\tan(\phi) = 2$ obtained in dissolution ($k_c^+ = 2 \times 10^{-3}$) is exactly the same for sublimation ($k_c^+ = 6.7 \times 10^{-3}$). Thus, the propagation angle of the transverse linear undulations appears to be constant, whether the substrate is ablated by sublimation or by dissolution. This allows us to confirm the similarity of these two ablation waves. The dissolution waves can therefore be used to complete the sublimation data set in order to validate scaling laws.

4.3 Validation and prediction

Scaling laws have been developed in sublimation by Bordiec et al. (2020) to relate the morphological and kinematic characteristics of sublimation waves to the characteristics of the environment in which they occur. Since the type of transfer does not affect the instability, the laws can be generalized and are valid for both sublimation and dissolution. However, previously (§4.2.2) shows that the characteristic numbers of the most unstable mode σ_c^+, ω_c^+ and k_c^+, related to the instability of the ablation waves are Schmidt number dependent. The point is that these characteristic numbers appear explicitly in the expressions of the physical quantities of interest such as wavelength, migration velocity and growth time. The objective of this section is therefore to compare these theoretical scaling laws with the terrestrial analogues and laboratory experiments described in §3 in the framework of a varying Schmidt number. The set of mean values of the parameters involved in the three scaling laws is summarized in **Table 2**. The values correspond either to measurements used for validation (white cells) or to predictions from the laws (grey cells). In order to verify the analogical character of the dissolution experiment with the terrestrial observations and the sublimation experiment, we now apply the scaling laws we have found numerically.

4.3.1 Wavelength

The first scaling law relates the wavelength λ to the viscous length $\frac{\nu}{u_*}$:

$$\frac{\nu}{u_*} Sc^{1/5} = \frac{\lambda}{2\pi} k^+_{c\,ref}, \tag{6}$$

where $k^+_{c\,ref} = 6.7 \times 10^{-3}$ is the dimensionless wavenumber of reference numerically obtained for $Sc = 1$ when the maximum growth rate is reached ($\sigma^+ = \sigma_c^+$). This first scaling law is represented by solid lines in **Figure 8A**. It is superposed with the measurements (symbols) made by other authors from natural and experimental data (Curl, 1966; Blumberg and Curl, 1974; Bintanja et al., 2001; Bordiec et al., 2020) for different Schmidt numbers (**Table 2**). This new formulation given by Eq. **6** allows to take into account the similarity between dissolution and sublimation measurements and to validate this law also by the laboratory experiments of dissolution waves presented in §3.3.2.

This law shows that the wavelength λ is inversely proportional to the friction velocity u_* for a given flow whatever the substrate: the faster the velocity, the smaller the wavelength. This is in accordance of what has been observed for sublimation waves on BIA's (Weller, 1969; Mellor and Swithinbank, 1989; Bintanja et al., 2001). For higher viscosity, depending on the pressure of the atmosphere as for instance Pluto's kinematic viscosity that is 40 times higher than martian's viscosity because of the lower pressure of the atmosphere, larger wavelength have to be found for comparable friction velocity at equivalent Schmidt number (~1). In this case, the ratio of the wavelength is directly proportional to the ratio of the viscosity: for sublimation wavelength about ~10 m on Mars, the corresponding wavelength for the same friction velocity of $u_* = 0.056\ \mathrm{m \cdot s^{-1}}$, is ~400 m on Pluto. The friction velocity can be predicted by the law, knowing the viscosity and the observed wavelength for these environment.

4.3.2 Migration velocity

The second scaling law proposed by Bordiec et al. (2020) related to the migration velocity of the ablation waves is proportional to the average value of the ablation rate $\frac{q^0}{\rho_s}$:

$$v_x = \frac{|\omega_c^+|}{k_c^+} \frac{q^0}{\rho_s}, \tag{7}$$

where $\frac{|\omega_c^+|}{k_c^+} \simeq 2$, not only for $Sc \simeq 1$, but also for a set of Schmidt numbers between 10^2 and 10^3 (**Figure 7C**). This explains why the law Eq. **7**, represented by solid line on **Figure 8B** is in line with the measurements on the natural and experimental systems (symbols) without taking into account the Schmidt number, revealing the analogue character of the dissolution experiments. The available measured data (**Table 2**, white cells) concern the sublimation ripples of the BIA's in Antarctica represented by blue

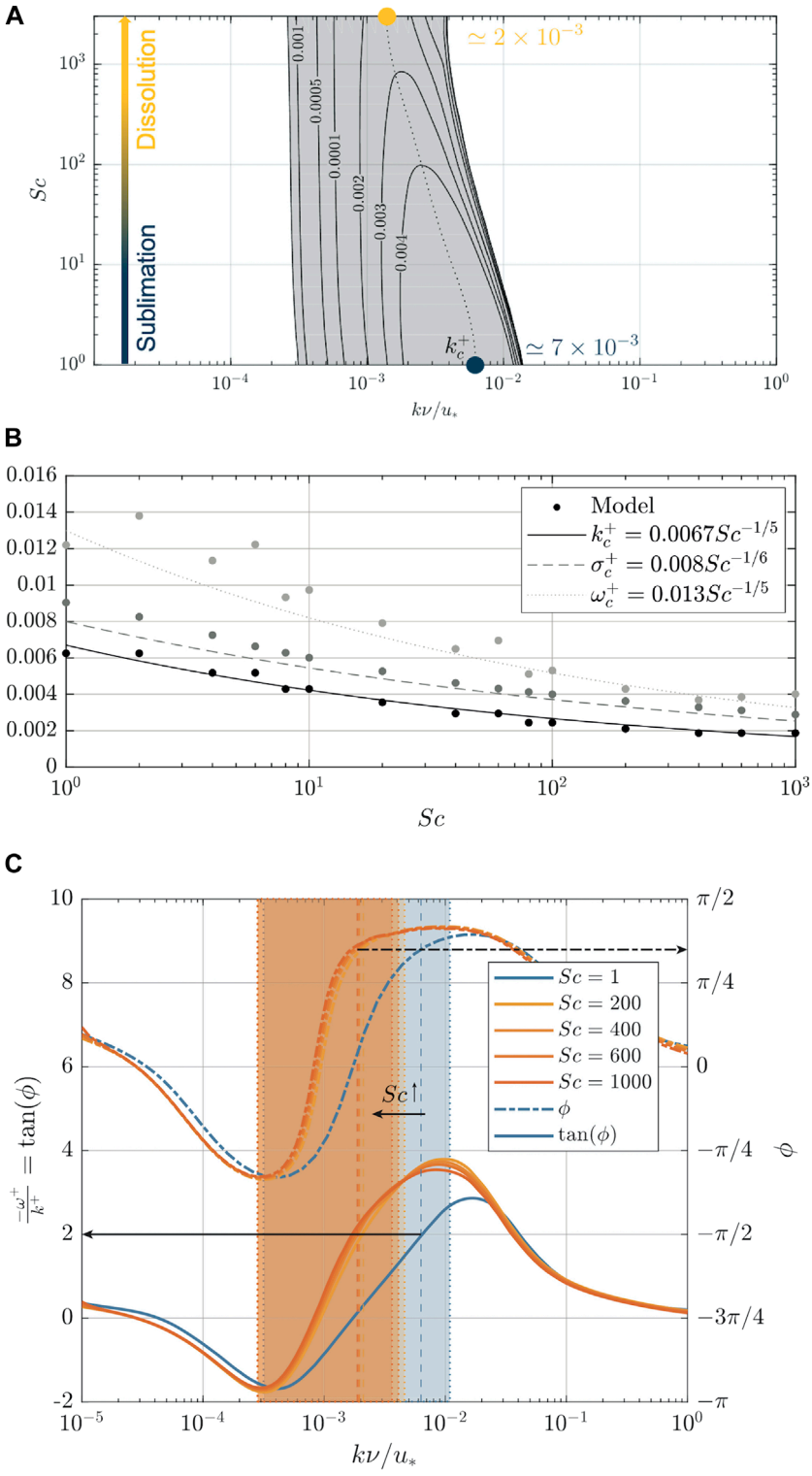

FIGURE 7
Influence of the Schmidt number on the dimensionless parameters of the dispersion relation. **(A)** Stability diagram in the (*Sc; kν/u**) plane. The shaded area corresponds to the unstable domain ($\sigma^+ > 0$) and the values displayed are those of the σ^+ isocontours. The dashed line represents the most unstable mode σ_c^+. **(B)** Evolution of the dimensionless parameters k_c^+, ω_c^+, σ_c^+, of the dispersion relation as a function of Schmidt number obtained from the model (symbols). Lines, dashed lines and dotted lines represent the best fit for each parameter (k_c^+, σ_c^+, ω_c^+, resp.). **(C)** Coefficient $-\omega^+/k^+$ as a function of the scaled wave number $k\nu/u_*$, for different Schmidt numbers. The solid lines correspond to tan(ϕ) (left axis) and the alternate lines to ϕ (right axis). The colors are associated with the Schmidt number. The colored areas are the areas of instability. The vertical dashed lines are the most amplified modes. Finally, the arrows indicate the value of tan(ϕ) and ϕ associated with the most amplified mode in each case.

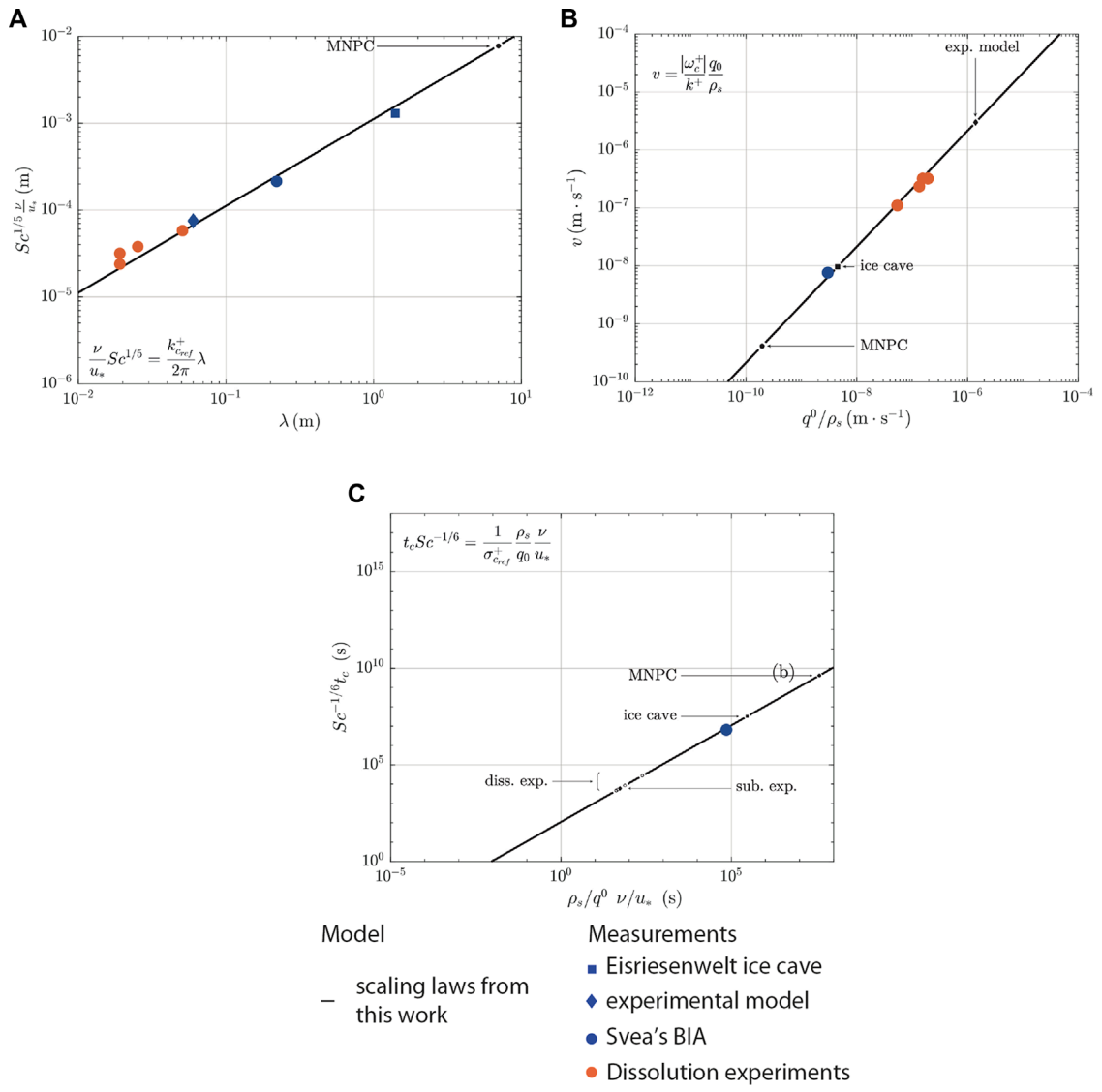

FIGURE 8
Scaling laws (black lines) for the unified model of sublimation waves on Earth (blue symbols: square = ice cave; circle = BIAs; diamond = CO_2 experiment) and dissolution waves (orange symbols). Symbols represent measured quantities, black dots are predictions. **(A)** First theoretical scaling law relating the wavelength λ to the viscous length ν/u_* (solid line), derived from the dispersion relation and superimposed on the measurements on sublimation waves (in blue) and on dissolution waves (in orange). The dependance on the Schmidt number is included to present an unified model. **(B)** Second theoretical scaling law relating the migration velocity v to the ablation rate q^0/ρ_s (solid line), derived from the dispersion relation and superimposed on the measurements (symbols) on the natural and experimental systems (orange for the dissolution experiment (Blumberg and Curl, 1974); blue for the BIAs (Bintanja et al., 2001)). The positions of the sublimation waves observed on the surface of the MNPC, in the ice cave of *Eisriesenwelt* and in the experimental model (v unknown because never measured) are indicated by black dots superimposed on the scaling law. The non-dependance on the Schmidt number shows the analogous character of dissolution waves as a terrestrial analogue of the sublimation waves. **(C)** Third theoretical scaling law relating the growth time t to the ablation rate q^0/ρ_s and the viscous length ν/u_* (solid line), derived from the dispersion relation and superimposed on the measurements on the unique measure natural system (on the BIAs (Bintanja et al., 2001)). The positions of the sublimation waves observed on the surface of the MNPC, in the ice cave of *Eisriesenwelt*, in the experimental model are indicated by black dots superimposed on the scaling law and for the dissolution experiment (Blumberg and Curl, 1974) are indicated by black circles superimposed on the scaling law. The dependance on the Schmidt number is included to present an unified model.

circles (Bintanja et al., 2001) and the dissolution waves in orange (Blumberg and Curl, 1974). Thanks to the analogue dissolution experiments, this law is validated both in sublimation and dissolution.

Because this law shows that the migration speed of these ablation waves depends only on the ablation rate (**Figure 8B**), the law can be used to predict the migration rate or, conversely, to estimate an ablation rate if the migration velocity is measured. For example, the predictions for the sublimation waves observed on the surface of the North Polar Cap of Mars, in the ice cave of *Eisriesenwelt* and in the experimental CO_2 model (**Table 2**, grey cells) are indicated by black dots superimposed on the

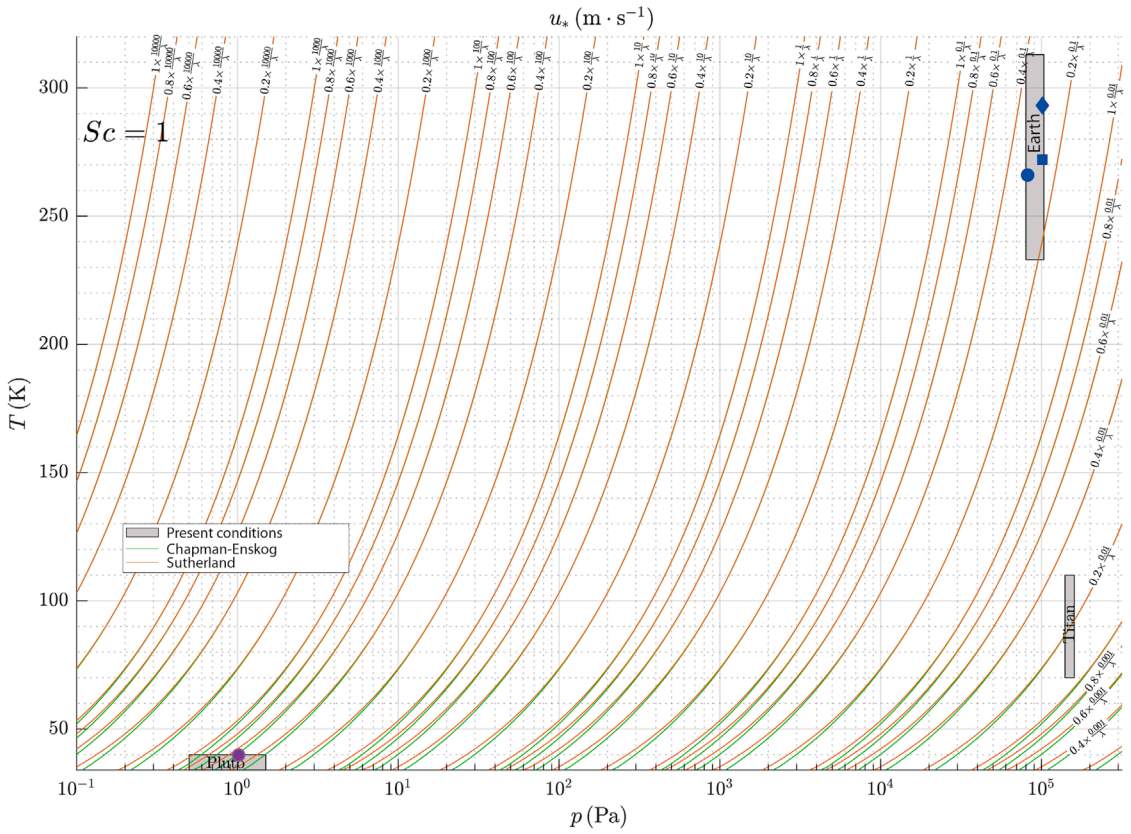

FIGURE 9
Graphical representation of the first law for sublimation in a N_2 rich atmosphere (Sc = 1). Knowing the wavelength of the sublimation waves, one can determine the friction velocity locating the ambient pressure and temperature over the wave field on the planetary body considered. The grey rectangles correspond to the pressure and temperature ranges for Earth, Titan and Pluto. The blue symbols correspond to the natural examples of sublimation ripples studied (square = ice cave; circle = BIAs; diamond = CO_2 experiment). The purple symbol is for Pluto.

scaling law. The predictions made where the migration velocity has not been measured are realistic for the ice cave and the CO_2 sublimation experiment but remain to be confirmed with further experiments or *in situ* campaign. Using the measured values of the propagation angle ϕ in the Blumberg and Curl (1974)'s experiments 1-4 ($\phi = 62°$; 60°; 59°; 64°, resp.), the migration velocities have been deduced geometrically (see **Figure 6B**) in **Table 2**, white cells. They are in perfect agreement with the predictions of the law for experiments 1-4 (1.1×10^{-7}, 2.6×10^{-7}, 3.4×10^{-7}, 3.3×10^{-7}, resp.).

4.3.3 Growth time

The third law relates the characteristic growth time to the viscous length and the ablation rate, and is therefore dependent on the flow and type of transfer (**Figure 8C**):

$$t_c Sc^{-1/6} = \frac{1}{\sigma^+_{c\,ref}} \frac{\rho_s}{q^0} \frac{\nu}{u_*}, \tag{8}$$

where $\sigma^+_{c\,ref} = 8.9 \times 10^{-3}$ is the maximum growth rate of reference obtained for $Sc = 1$. The growth time represents the spontaneous emergence of the ablation waves from an initially flat surface. It constitutes a interesting tool for assessing the order of magnitude of the time scale of development of ablation waves on a solid substrate and to link their growth to their ablation rates. Hence, the law remains a tool for estimating the potential age of surfaces. The predictions are possible but still lack data to confirm them, which could be obtained experimentally. The predicted times for the sublimation of CO_2 ice experiments and the dissolution experiments (**Table 2**) show that they are feasible in practice at the laboratory time scale with characteristic growth times between 1.5 and 20 h. Consequently, this is the approach that should be favored to validate this law because natural examples develop over far too long a period of time. Indeed, the only available measurement for this characteristic growth time is given in Antarctica (**Table 2**) where ripples appear in 74 days, which is consistent with the predictions ~85 days. It would take about 1 year for the sublimation waves to be fully developped in the *Eisriesenwelt* ice caves. For Mars on the MNPC, by setting an average of 35 sols of pure sublimation to have an order of magnitude, it would thus take 44,000 sols to observe well-shaped sublimation waves, which corresponds to about 1,200 Martian years for these landforms to grow. This very large time frame makes it possible to use these sublimation waves as markers of erosion zones on the MNPC as well as for Pluto where growth time are even longer.

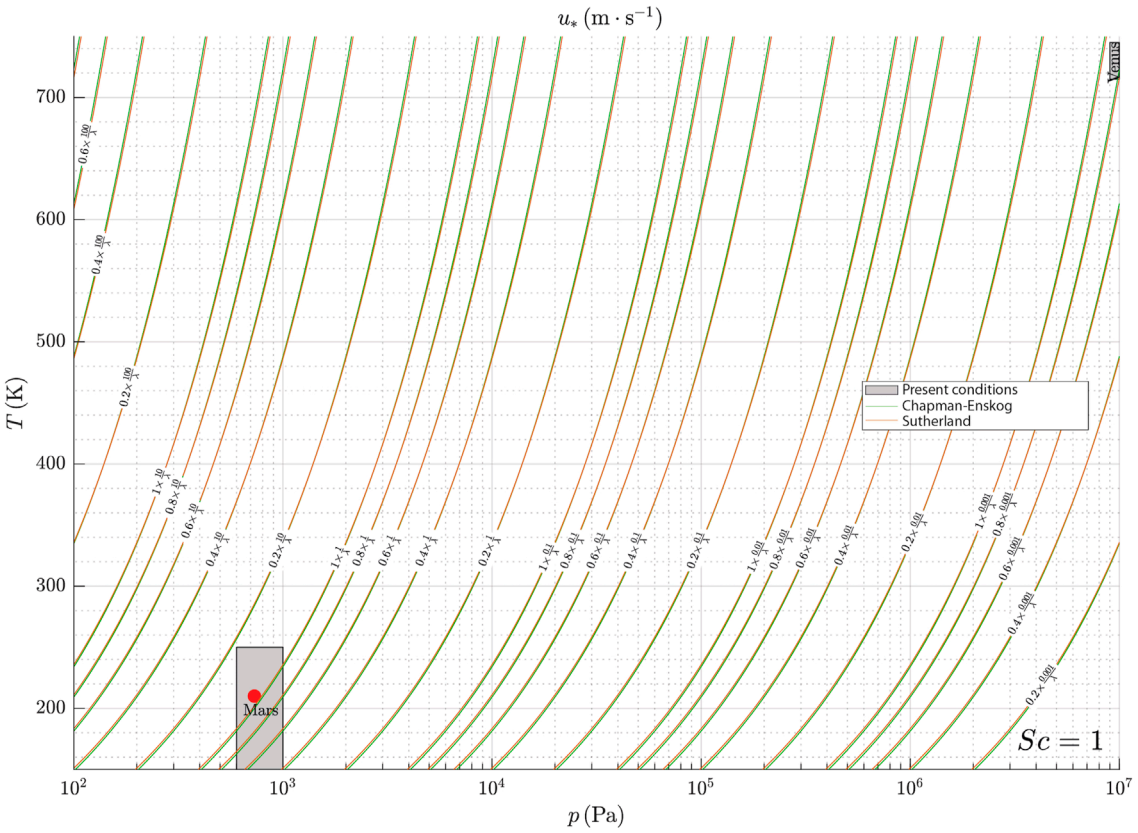

FIGURE 10
Graphical representation of the first law for sublimation in a CO_2 rich atmosphere (Sc = 1). Knowing the wavelength of the sublimation waves, one can determine the friction velocity locating the ambient pressure and temperature over the wave field on the planetary body considered. The grey rectangles correspond to the pressure and temperature ranges for Mars and Venus. The red circle represents the environmental condition over the sublimation waves that have been identified on the MNPC.

5 Charts for estimating friction velocity in different environments

The scaling laws presented in the previous section §4 have been developed to propose a unified model of ablation waves for dissolution and sublimation. To create a tool for the direct application of the laws in environments as diverse as ice caves, icy surfaces, laboratory experiments, planetary surfaces, karsts and limestone, gypsum and halite surfaces, we present these results in the form of specific charts. Since the coefficients k_c+, ω_c+ and σ_c+ of the laws differ in dissolution and in sublimation, we design a graphical representation of family of curves for each type of transfer: **Figures 9, 10** for sublimation, depending on the composition of the atmosphere (**Table 1**); **Figure 12** for dissolution.

Considering that the basic quantities measured and/or measurable in the application environments consist mainly of ambient pressure and temperature (**Table 2**), the calculations to obtain the family of curves have to be adapted to these two parameters. For exemple in **Figure 12**, by plotting the temperature of water at ambient pressure, it is possible to estimate u_* thanks to the first scaling law (Eq. **6**) if a measure of λ of dissolution waves exists and *vice versa*. This presupposes an implicit calculation of the viscosity following different viscosity laws (e.g. *Sutherland* and *Chapman-Enskog*, Chapman et al. (1990)). In most cases, the choice of the viscosity law does not affect these estimates because the *Sutherland* and *Chapman-Enskog* laws are superimposed for the mean pressure and temperature ranges concerned in most of the relevant planetary environments (**Figure 1**, grey boxes, $p > 10^{-2}$ Pa). In sublimation, and by using the first law, the friction velocity can be represented as a function of pressure, temperature and observed wavelength, for all N_2-rich atmospheres in **Figure 9**. This allows application to the Earth, Titan or Pluto. CO_2-rich atmospheres in **Figure 10** allow applications to Venus and Mars.

The other two laws (Eq. **7**, **8**) are more difficult to represent graphically as a function of pressure and temperature alone. Indeed, these laws imply the ablation rate that can only be constrained on the condition of knowing the temperature T, the pressure p but also the temperature at the interface T_{int} and a value of relative or specific humidity in the case of sublimation, and the temperature, the solubility, the concentration and the pH in the case of dissolution. To simplify the representation of these laws, they can be combined to give:

$$\frac{q^0}{\rho_s} = \frac{k_c^+}{2\pi\sigma_c^+}\frac{\lambda}{t_c}, \tag{9}$$

$$v_x = \frac{|\omega_c^+|}{2\pi\sigma_c^+}\frac{\lambda}{t_c}. \tag{10}$$

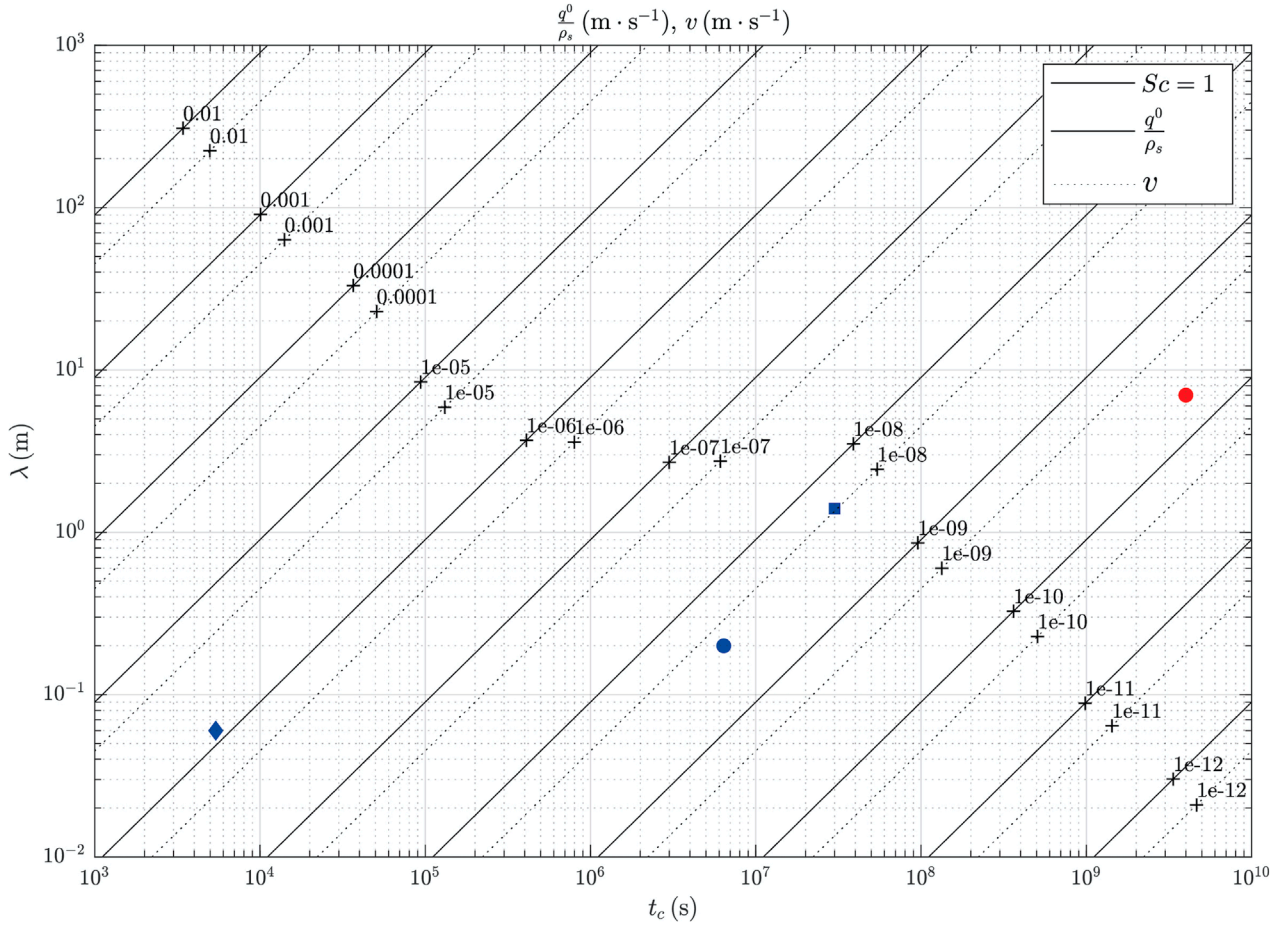

FIGURE 11
Combination of the second and third laws for sublimation (*Sc* =1). Locating the wavelength on the y-axis and drawing a line upward to the curve representing the sublimation rate or the migration velocity, the formation time can be determined by reading thanks to a line drawn vertically. The blue symbols represent the natural examples of sublimation ripples studied (square = ice cave; circle = BIAs; diamond = CO_2 experiment) and the red circle represents the sublimation waves identified on the MNPC.

with $k_c^+ = k_{c\,ref}^+ Sc^{-1/5}$ and $\omega_c^+ = \omega_{c\,ref}^+ Sc^{-1/5}$. Thus, the ablation rate and the migration velocity can be plotted on the same graph.

5.1 Application to sublimation waves

In icy planetary environments potentially subject to sublimation (§2.2, **Table 1**), the main gases involved are nitrogen N_2 and carbon dioxide CO_2. Two charts are proposed for atmospheres rich in N_2 (**Figure 9**) and CO_2 (**Figure 10**). The viscosity of these gases as a function of temperature is relatively well known at standard pressures. This is why a first tool to deduce $u_\star$ and/or λ is proposed from the knowledge of temperature and pressure. The possible ranges of variation in p and T in the current configuration of each planetary environment are represented by grey areas on **Figures 9, 10**. Except for Pluto, where pressure changes induce strong viscosity variations, the number of curves crossing the environments is generally small, that induces reduced possibilities of $u_\star - \lambda$ combinations at given pressure and temperature.

The natural examples (BIAs, ice cave) and laboratory experiments of CO_2 ice presented in §2.3.1 and §2.3.2 are plotted on **Figure 9** (see blue symbols) for N_2-rich atmospheres. It makes thus possible to find an estimate of $u_\star$ or λ. For the sublimation waves observed on the MNPC in §2.3.3 (red symbol in **Figure 10**), knowing the average atmospheric pressure and the temperature near the surface (**Table 2**) where they have been observed, one can obtain the friction velocity, simply by replacing λ by its value. The value extracted from the corresponding curve is $u_\star \sim \frac{0.6}{\lambda}$ thanks to the environments conditions. The calculation of $u_\star \sim 0.085$ m · s^{-1} with the measured $\lambda = 7$ m is in agreement with the predictions for the friction velocity derived from the Martian Climate Database (Forget et al., 1999; Head et al., 2003; Millour et al., 2018) over the region described in §2.3.3.

In **Figure 9**, the current conditions of Pluto have been indicated by a purple circle in the grey area. The same application as above to the observed wavelength of Sputnik Planitia in §2.3.4 gives $u_\star = 0.4\frac{100}{\lambda}$, using the most realistic viscosity laws (*i.e Sutherland* and *Chapman-Enskog*). These two different viscosity laws are used to show the potential influence of the choice of their use, for certain ranges of pressure and temperature. Nevertheless, the values extracted from the curve thanks to the environment condition and the measure of λ are in agreement with the predictions from other

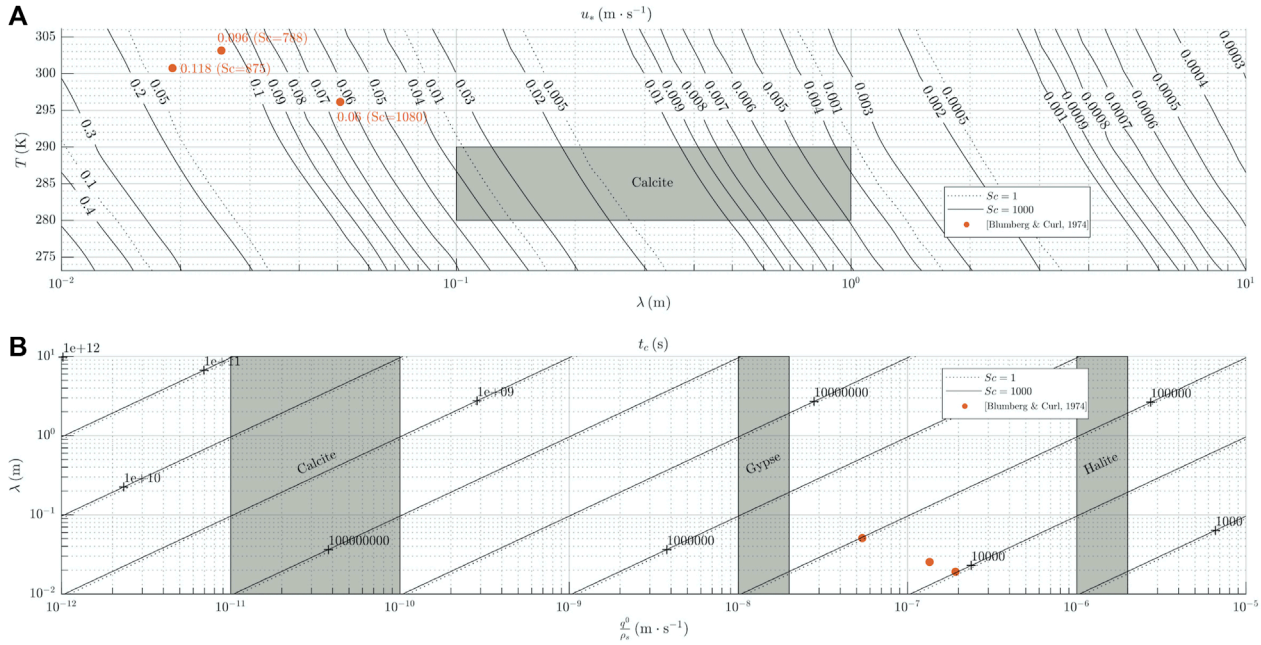

FIGURE 12
Dissolution of rocks soluble in liquid water. The shaded areas correspond to typical ranges of temperature and dissolution rates encountered in natural environments. The orange circles represent the experimental results of Blumberg and Curl (1974). **(A)** First law **(B)** Combination of second and third law.

works (Forget et al., 2017) for Pluto. For wavelengths in the range of $0.4 < \lambda < 1$ km, friction velocity is such that $0.04 < u_* < 0.1$ m · s^{-1} noting that lower velocity values are obtained where the walengths are larger. This result is much lower than the friction velocity thresholds estimated for grain transport (Telfer et al., 2018; Gunn and Jerolmack, 2022). Since the strongest winds are expected to be where the topographic gradients are greatest, the northwestern part of Sputnik Planitia would correspond to a more windy region and the regions where the wavelength more widely spaced to more moderate winds. This typical behaviour combined to the wavelength of the sublimation waves that seems to be linked to the viscosity on Pluto 40× greater than on Mars, that could explain the difference in scale observed in these two environments, suggest that the waves observed on the northwest of Sputnik Planitia could be reinterpreted as sublimation waves.

The combination of scaling laws allows the ablation and the migration rates to be plotted on the same graph, independently of the nature of the substrate and the flow. Reading **Figure 11** then allows to know the growth time t_c from the knowledge of the ablation rate and the wavelength or from the migration velocity and the wavelength. This is relevant for the surfaces of BIAs and on the North Polar Cap of Mars. For the special case of ice caves, where the estimation of the sublimation rate is more difficult, it can be obtained by knowing the growth time and the wavelength.

The different validated applications are shown on **Figure 11** (see blue and red symbols). As the data collected are isolated points in their parameter scale, given that the environmental conditions and sometimes even the type of icy substrate are different, there is no systematic measurements of bedform's wavelength change when continuously varying some control parameter. In order to investigate a range of wind velocity and fluid viscosity in a controlled environment, this chart will be helpful tool for scaling laboratory experiments of sublimation. Such experiments would make it possible to characterize these sublimation waves in terms of their growth time, ablation rate and migration velocity.

5.2 Application to dissolution waves

The dissolution rates of limestone, gypsum and halite are widely studied and constrained in various situations (**Table 3**). The dissolution takes place in water whose viscosity depends mainly on temperature (Kaufmann et al., 2014). Since the temperatures concerned by this type of reaction are temperatures for which the kinematic viscosity of pure water is well known, the viscosity is injected directly into the law. Despite the lack of existing data, Blumberg and Curl (1974)'s experiments (§3.3.2) allow the abacus chart to be validated by entering the values of **Table 2** in the form of red symbols in **Figure 12A**. Choosing this type of graphical representation constitutes a tool for finding the friction velocity u_* and the velocity of the flow by extrapolation (Bordiec et al., 2020), as a function of the temperature on the one side and the measurement of a wavelength on the other side. A quick application to the transverse linear undulations observed in the Cave of *St-Marcel d'Ardèche* (§3.3.1) assuming that $Sc = 1{,}000$ and that the temperature is of the order of $T = 10$°C, the friction velocity u_* from figure **Figure 12** is $\simeq 0.06$ m · s^{-1}, which leads to a very low flow velocity at $z = 1$ m of the wall of the order of $u_x(z = 1\text{ m}) \simeq 1$ cm · s^{-1}.

This tool is also useful for the design of new experiments, choosing a couple (u_*, T), one can then define the desired wavelength range allowing a scaling of the experiment on an adapted exposure time. We propose to design the chart for dissolution in order to

obtain the exposure times of surfaces to a water flow, knowing from Eq. (9) that:

$$t_c = \frac{k_c^+}{2\pi\sigma_c^+}\lambda\frac{\rho_s}{q^0} \tag{11}$$

This is relevant to estimate formation time of the dissolution waves (**Figure 12B**) in the experiments or in natural exemples. For example, the chart does provide growth times of between 4 h and 20 h for the wavelengths obtained by Blumberg and Curl (1974). With the same wavelength and similar hydrodynamic conditions, the growth time, induced by the rate of dissolution, is therefore naturally 100 times greater for calcite than for gypsum, itself 100 times greater than for halite. Considering an average estimate of the calcite dissolution rate such that $q^0/\rho_s \simeq 4\times10^{-11}$ (**Table 3**), the chart provides a characteristic growth time of the dissolution waves of the walls of *Grotte de St-Marcel* of the order of $\simeq 100$ years. This enables an estimation of the required minimum residence time for water to form this type of beforms, but also an idea of the velocity of the paleo-flow as a function of the observed wavelength.

6 Conclusion

The development of transverse linear ablation bedforms, either by dissolution or sublimation of solid substrates, can be unified in a single analytical model that couples mass transfers and near-wall turbulent flow. The linear stability analysis of the model shows that the propagation angle, defined as the ratio between the ablation rate and the migration velocity, is equal to $\simeq 60°$ for both ablation processes. By contrast, the coefficients of the dispersion relation differ between sublimation and ablation dissolution, because these different ablation processes involve different values of the Schmidt number. Three scaling laws derived from the model relate the geometric and kinematic characteristics of ablation waves to the characteristics of the environment in which they form: (i) bedform wavelengths are related to the ratio viscosity over friction velocity, (ii) bedform migration velocities are related to ablation rates, (iii) bedform characteristic growth times are related to viscous lengths and ablation rates. These scaling laws correctly fit a set of data measured on ablation waves on soluble rocks (by dissolution) and on volatile ices (by sublimation) in terrestrial, extra-terrestrial and experimental settings. They can be used to predict flow velocities, ablation rates and characteristic growth times for other ablation waves. Specific charts derived from the laws allow the model predictions to be used to design new experiments and to be extended to other terrestrial and planetary ablation waves.

Data availability statement

The original contributions presented in the study are included in the article/supplementary material, further inquiries can be directed to the corresponding author.

Author contributions

As a physicist, SC has proposed a unified model for the scaling laws for ablation waves in sublimation and dissolution based on the modeling of the coupled equations developed by MB. As a planetary geomorphologist, OB has contributed to find natural examples of sublimation and dissolution waves in order to validate the model. He has conducted the field trip expedition in the Saint Marcel cave. All authors contributed to the article and approved the submitted version.

Funding

TelluS programme of the INSU (CNRS) SYSTER Action 2019, in the framework of the project "Characterisation and modelling of periodic dissolution forms on limestone walls subjected to water flows". National Planetology Plan programme of the INSU (CNRS) Action 2021, in the framework of the project "OnDiNE" that aim to design specific charts for sublimation waves experiments. This project has been supported by the Observatory of the sciences of the Universe Nantes Atlantique (Osuna, Nantes University, CNRS UAR-3281, UGE, CNAM, univ Angers, IMT Atlantique) and Région Pays de la Loire.

Acknowledgments

We acknowledge Delphine Dupuy, in charge of preservation and valorization of cultural heritage at the Saint Marcel's cave, France; Stéphane Bonnet (GET, Toulouse, France) and Marion Massé (LPG, Nantes, France) for LIDAR acquisition in the cave; we acknowledge for scientific discussions Philippe Claudin (PMMH, Paris, France) and "les Treilles, atelier dunes" Team. We acknowledge the reviewers for their constructive feedbacks that allow to improve significantly the clarity and quality of the manuscript.

Conflict of interest

The authors declare that the research was conducted in the absence of any commercial or financial relationships that could be construed as a potential conflict of interest.

Publisher's note

References

Allen, J. R. (1971). Transverse erosional marks of mud and rock: Their physical basis and geological significance. *Sediment. Geol.* 5, 167–385. doi:10.1016/0037-0738(71)90001-7

Altwegg, K., Balsiger, H., Bar-Nun, A., Berthelier, J. J., Bieler, A., Bochsler, P., et al. (2015). Cometary science. 67P/Churyumov-Gerasimenko, a Jupiter family comet with a high D/H ratio. *Science* 347, 1261952. doi:10.1126/science.1261952

Anderson, J. D., Lau, E. L., Sjogren, W. L., Schubert, G., and Moore, W. (1996). Gravitational constraints on the internal structure of Ganymede. *Nature* 384, 541–543. doi:10.1038/384541a0

Baker, V. R. (2001). Water and the martian landscape. *Nature* 412, 228–236. doi:10.1038/35084172

Banks, M. E., Byrne, S., Galla, K., McEwen, A. S., Bray, V. J., Dundas, C. M., et al. (2010). Crater population and resurfacing of the Martian north polar layered deposits. *J. Geophys. Res. E Planets* 115, E08006. doi:10.1029/2009JE003523

Bertrand, T., Forget, F., Umurhan, O. M., Grundy, W. M., Schmitt, B., Protopapa, S., et al. (2018). The nitrogen cycles on Pluto over seasonal and astronomical timescales. *Icarus* 309, 277–296. doi:10.1016/j.icarus.2018.03.012

Bertrand, T., Forget, F., Umurhan, O. M., Moore, J. M., Young, L. A., Protopapa, S., et al. (2019). The CH 4 cycles on Pluto over seasonal and astronomical timescales. *Icarus* 329, 148–165. doi:10.1016/j.icarus.2019.02.007

Bertrand, T., Forget, F., White, O., Schmitt, B., Stern, S. A., Weaver, H. A., et al. (2020). Pluto's beating heart regulates the atmospheric circulation: Results from high-resolution and multiyear numerical climate simulations. *J. Geophys. Res. Planets* 125, e2019JE006120. doi:10.1029/2019je006120

Bertrand, T., Lellouch, E., Holler, B., Young, L., Schmitt, B., Marques Oliveira, J., et al. (2022). Volatile transport modeling on triton with new observational constraints. *Icarus* 373, 114764. doi:10.1016/j.icarus.2021.114764

Bintanja, R. (1999). On the glaciological, meteorological, and climatological significance of antarctic blue ice areas. *Rev. Geophys.* 37, 337–359. doi:10.1029/1999RG900007

Bintanja, R., Reijmer, C. H., and Hulscher, S. J. (2001). Detailed observations of the rippled surface of Antarctic blue-ice areas. *J. Glaciol.* 47, 387–396. doi:10.3189/172756501781832106

Blumberg, P. N., and Curl, R. L. (1974). Experimental and theoretical studies of dissolution roughness. *J. Fluid Mech.* 65, 735–751. doi:10.1017/S0022112074001625

Bordiec, M., Carpy, S., Bourgeois, O., Herny, C., Massé, M., Perret, L., et al. (2020). Sublimation waves: Geomorphic markers of interactions between icy planetary surfaces and winds. *Earth-Science Rev.* 211, 103350. doi:10.1016/j.earscirev.2020.103350

Byrne, S., and Ingersoll, A. P. (2003). A sublimation model for martian South Polar ice features. *Science* 299, 1051–1053. doi:10.1126/science.1080148

Byrne, S. (2009). The polar deposits of mars. *Annu. Rev. Earth Planet. Sci.* 37, 535–560. doi:10.1146/annurev.earth.031208.100101

Carroll, M. (2019). "Ceres: The first known ice dwarf planet," in *Ice worlds of the solar system* (Berlin, Germany: Springer). doi:10.1007/978-3-030-28120-5_4

Chapman, S., Cowling, T. G., Burnett, D., and Cercignani, C. (1990). *The mathematical theory of non-uniform gases: An account of the kinetic theory of viscosity, thermal conduction and diffusion in gases*. Cambridge, UK: Cambridge Mathematical Library, Cambridge University Press.

Chittenden, J. D., Chevrier, V., Roe, L. A., Bryson, K., Pilgrim, R., and Sears, D. W. G. (2008). Experimental study of the effect of wind on the stability of water ice on Mars. *Icarus* 196, 477–487. doi:10.1016/j.icarus.2008.01.016

Claudin, P., Durán, O., and Andreotti, B. (2017). Dissolution instability and roughening transition. *J. Fluid Mech.* 832, R2–832R214. doi:10.1017/jfm.2017.711

Colombani, J., and Bert, J. (2007). Holographic interferometry study of the dissolution and diffusion of gypsum in water. *Geochimica Cosmochimica Acta* 71, 1913–1920. doi:10.1016/j.gca.2007.01.012

Conway, S. J., Hovius, N., Barnie, T., Besserer, J., Le Mouélic, S., Orosei, R., et al. (2012). Climate-driven deposition of water ice and the formation of mounds in craters in Mars' north polar region. *Icarus* 220, 174–193. doi:10.1016/j.icarus.2012.04.021

Courrech du Pont, S., Narteau, C., and Gao, X. (2014). Two modes for dune orientation. *Geology* 42, 743–746. doi:10.1130/G35657.1

Cruikshank, D. P., Howell, R., Geballe, T., and Fanale, F. (1985). "Sulfur dioxide ice on Io," in *Ices in the solar system*. Editor J. Klinger (Netherlands: Springer), 805–815. chap. Cruikshank. doi:10.1007/978-94-009-5418-2_55

Cubillas, P., Köhler, S., Prieto, M., Causserand, C., and Oelkers, E. H. (2005). How do mineral coatings affect dissolution rates? An experimental study of coupled CaCO3 dissolution - CdCO3 precipitation. *Geochimica Cosmochimica Acta* 69, 5459–5476. doi:10.1016/j.gca.2005.07.016

Curl, R. L. (1966). Scallops and flutes. *Trans. Cave Res. Group G. B.* 7, 121–160.

Daupley, X., Laouafa, F., Billiotte, J., and Quintard, M. (2015). "La dissolution du gypse: Quantifier les phénomènes," in *Mines and carrières hors-série*, 35–43.

Deutsch, A. N., Neumann, G. A., and Head, J. W. (2017). New evidence for surface water ice in small-scale cold traps and in three large craters at the north polar region of Mercury from the Mercury Laser Altimeter. *Geophys. Res. Lett.* 44, 9233–9241. doi:10.1002/2017GL074723

Dougherty, M., Khurana, K., Neubauer, F., Russell, C. T., Saur, J., Leisner, J., et al. (2006). Identification of a dynamic atmosphere at Enceladus with the cassini magnetometer. *Science* 311, 1406–1409. doi:10.1126/science.1120985

Durán, O., Andreotti, B., Claudin, P., and Winter, C. (2019). A unified model of ripples and dunes in water and planetary environments. *Nat. Geosci.* 12, 345–350. doi:10.1038/s41561-019-0336-4

Eke, V. R., Lawrence, D. J., and Teodoro, L. F. (2017). How thick are Mercury's polar water ice deposits? *Icarus* 284, 407–415. doi:10.1016/j.icarus.2016.12.001

Ernst, C. M., Chabot, N. L., and Barnouin, O. S. (2018). Examining the potential contribution of the hokusai impact to water ice on Mercury. *J. Geophys. Res. Planets* 123, 2628–2646. doi:10.1029/2018JE005552

Fanale, F. P., Postawko, S. E., Pollack, J. B., Carr, M. H., and Pepin, R. O. (1992). "Mars: Epochal climate change and volatile history," in *Mars*. Editor M. George, 1135–1179.

Ford, D. C., and Williams, P. (1989). *Karst geomorphology and hydrology*. Netherlands: Springer.

Forget, F., Bertrand, T., Vangvichith, M., Leconte, J., Millour, E., and Lellouch, E. (2017). A post-new horizons global climate model of Pluto including the N2, CH4 and CO cycles. *Icarus* 287, 54–71. doi:10.1016/j.icarus.2016.11.038

Forget, F., Hourdin, F., and Dalagrand, O. (1999). Improved general circulation models of the Martian atmosphere from the surface to above 80 km. *J. Geophys. Res. – Planets (E)* 104, 24,155–24,175. doi:10.1029/1999JE001025

Frumkin, A. (1994). Hydrology and denudation rates of halite karst. *J. Hydrology* 162, 171–189. doi:10.1016/0022-1694(94)90010-8

Frumkin, A. (2013). *Salt karst*, 6. Amsterdam, Netherlands: Elsevier Ltd. doi:10.1016/B978-0-12-374739-6.00113-5

Gallaire, F., and Brun, P. T. (2017). Fluid dynamic instabilities: Theory and application to pattern forming in complex media. *Philosophical Trans. R. Soc. A Math. Phys. Eng. Sci.* 375, 20160155. doi:10.1098/rsta.2016.0155

Ginés, A., Knez, M., Slabe, T., and Dreybrodt, W. (2009). *Karst rock features: Karren sculpturing*.

Goodchild, M., and Ford, D. C. (1972). Analysis of scallop patterns by simulation under controlled conditions: A discussion. *J. Geol.* 80, 121–122. doi:10.1086/627717

Grundy, W. M., Binzel, R. P., Buratti, B. J., Cook, J. C., Cruikshank, D. P., Dalle Ore, C. M., et al. (2016). Surface compositions across pluto and Charon. *Science* 351, aad9189. doi:10.1126/science.aad9189

Grundy, W. M., and Fink, U. (1991). A new spectrum of triton near the time of the voyager encounter. *Icarus* 93, 379–385. doi:10.1016/0019-1035(91)90220-N

Gulkis, S., Allen, M., Von Allmen, P., Beaudin, G., Biver, N., Bockelée-Morvan, D., et al. (2015). Cometary science. Subsurface properties and early activity of comet 67P/Churyumov-Gerasimenko. *Science* 347, aaa0709–6. doi:10.1126/science.aaa0709

Gunn, A., and Jerolmack, D. J. (2022). Conditions for aeolian transport in the solar system. *Nat. Astron.* 6, 923–929. doi:10.1038/s41550-022-01669-0

Hagedorn, B., Sletten, R. S., and Hallet, B. (2007). Sublimation and ice condensation in hyperarid soils: Modeling results using field data from victoria valley, Antarctica. *J. Geophys. Res. Earth Surf.* 112, F03017. doi:10.1029/2006JF000580

Hammer, O., Lauritzen, S. E., and Jamtveit, B. (2011). Stability of dissolution flutes under turbulent flow. *J. Cave Karst Stud.* 73, 181–186. doi:10.4311/2011JCKS0200

Hanratty, T. J. (1981). Stability of surfaces that are dissolving or being formed by convective diffusion. *Annu. Rev. Fluid Mech.* 13, 231–252. doi:10.1146/annurev.fl.13.010181.001311

Hayes, A. G. (2016). The lakes and seas of titan. *Annu. Rev. Earth Planet. Sci.* 44, 57–83. doi:10.1146/annurev-earth-060115-012247

Head, J. W., Mustard, J. F., Kreslavsky, M. A., Milliken, R. E., and Marchant, D. R. (2003). Recent ice ages on Mars. *Nature* 426, 797–802. doi:10.1038/nature02114

Herny, C., Massé, M., Bourgeois, O., Carpy, S., Le Mouélic, S., Appéré, T., et al. (2014). Sedimentation waves on the martian North Polar cap: Analogy with megadunes in Antarctica. *Earth Planet. Sci. Lett.* 403, 56–66. doi:10.1016/j.epsl.2014.06.033

Hofstadter, M. D., and Murray, B. C. (1990). Ice sublimation and rheology: Implications for the martian polar layered deposits. *Icarus* 84, 352–361. doi:10.1016/0019-1035(90)90043-9

Howard, A. D. (2000). The role of eolian processes in forming surface features of the martian polar layered deposits. *Icarus* 144, 267–288. doi:10.1006/icar.1999.6305

Incropera, F. P., Lavine, A. S., Bergman, T. L., and DeWitt, D. P. (2007). *Fundamentals of heat and mass transfer*. 6 edn. New York, United States: Wiley.

Ivanov, A. B., and Muhleman, D. O. (2000). The role of sublimation for the formation of the northern ice cap: Results from the mars orbiter laser altimeter. *Icarus* 144, 436–448. doi:10.1006/icar.1999.6304

Jakirlić, S., Manceau, R., Šarić, S., Fadai-Ghotbi, A., Kniesner, B., Carpy, S., et al. (2009). *LES, zonal and seamless hybrid LES/RANS: Rationale and application to free and wall-bounded flows involving separation and swirl*. Berlin, Heidelberg: Springer, 253–282. doi:10.1007/978-3-540-89956-3_11

Jakosky, B. M. (1985). The seasonal cycle of water on Mars. *Space Sci. Rev.* 41, 131–200. doi:10.1007/BF00241348

James, P. B., and North, G. R. (1982). The seasonal CO2 cycle on mars: An application of an energy balance climate model. *J. Geophys. Res.* 87, 10271–10283. doi:10.1029/JB087iB12p10271

Kaufmann, G., Gabrovšek, F., and Romanov, D. (2014). Deep conduit flow in karst aquifers revisited. *Water Resour. Res.* 50, 4821–4836. doi:10.1002/2014WR015314

Kauhanen, J., Siili, T., Ja, S., and Savija, H. (2008). The Mars limited area model and simulations of atmospheric circulations for the Phoenix landing area and season of operation. *J. Geophys. Res.* 113, E00A14. doi:10.1029/2007JE003011

Kelly, N. J., Boynton, W. V., Kerry, K. E., Hamara, D., Janes, D. M., Reddy, R. C., et al. (2007). Seasonal polar carbon dioxide frost on Mars: Co2 mass and columnar thickness distribution. *J. Geophys. Res. E Planets* 112, E03S07–12. doi:10.1029/2006JE002678

Khurana, K. K., Kivelson, M. G., Stevenson, D., Schubert, G., Russell, C., Walker, R. J., et al. (1998). Induced magnetic fields as evidence for subsurface oceans in Europa and Callisto. *Nature* 395, 777–780. doi:10.1038/27394

Kieffer, H. H., Chase, S. C., Martin, T. Z., Miner, E. D., and Palluconi, F. D. (1976). Martian North Pole summer temperatures: Dirty water ice. *Sci. (New York, N.Y.)* 194, 1341–1344. doi:10.1126/science.194.4271.1341

Kivelson, M. G., Khurana, K. K., Russer, C. T., Volwerk, M., Walker, R. J., and Zimmer, C. (2000). Galileo magnetometer measurements: A stronger case for a subsurface ocean at Europa. *Science* 289, 1340–1343. doi:10.1126/science.289.5483.1340

Knotek, S., and Jícha, M. (2014). Modeling of shear stress and pressure acting on small-amplitude wavy surface in channels with turbulent flow. *Appl. Math. Model.* 38, 3929–3944. doi:10.1016/j.apm.2013.11.065

Kreslavsky, M. A., and Head, J. W. (2002a). Fate of outflow channel effluents in the northern lowlands of Mars: The vastitas borealis formation as a sublimation residue from frozen ponded bodies of water. *J. Geophys. Res. Planets* 107, 4-1–4-25. doi:10.1029/2001JE001831

Kreslavsky, M. A., and Head, J. W. (2002b). Mars: Nature and evolution of young latitude-dependent water-ice-rich mantle. *Geophys. Res. Lett.* 29, 14-1–14-4. doi:10.1029/2002GL015392

Kreslavsly, M. A., and Bondarenko, N. V. (2017). Aeolian sand transport and aeolian deposits on Venus: A review. *Aeolian Res.* 26, 29–46. doi:10.1016/j.aeolia.2016.06.001

Kuzan, J. D., Hanratty, T. J., and Adrian, R. J. (1989). Turbulent flows with incipient separation over solid waves. *Exp. Fluids* 7, 88–98. doi:10.1007/BF00207300

Law, J., and Van Dijk, D. (1994). Sublimation as a geomorphic process: A review. *Permafr. Periglac. Process.* 5, 237–249. doi:10.1002/ppp.3430050404

Lee, C., Lewis, S. R., and Read, P. L. (2010). A bulk cloud parameterization in a Venus general circulation model. *Icarus* 206, 662–668. doi:10.1016/j.icarus.2009.09.017

Lellouch, E., de Bergh, C., Sicardy, B., Ferron, S., and Käufl, H.-U. (2010). Detection of co in triton's atmosphere and the nature of surface-atmosphere interactions. *A&A* 512, L8. doi:10.1051/0004-6361/201014339

Li, S., Lucey, P. G., Milliken, R. E., Hayne, P. O., Fisher, E., Williams, J. P., et al. (2018). Direct evidence of surface exposed water ice in the lunar polar regions. *Proc. Natl. Acad. Sci. U. S. A.* 115, 8907–8912. doi:10.1073/pnas.1802345115

Lopes, R. M., Wall, S. D., Elachi, C., Birch, S., Corlies, P., Coustenis, A., et al. (2019). Titan as revealed by the cassini radar. *Space Sci. Rev.* 215, 33. doi:10.1007/s11214-019-0598-6

Lunine, J. I., and Atreya, S. K. (2008). The methane cycle on Titan. *Nat. Geosci.* 1, 159–164. doi:10.1038/ngeo125

Malin, M. C., and Edgett, K. S. (2001). Mars global surveyor mars orbiter camera: Interplanetary cruise through primary mission. *J. Geophys. Res.* 106, 23429,429–23570,570. doi:10.1029/2000JE001455

Manceau, R., Carpy, S., and Alfano, D. (2002). "A rescaled v2?f model: First application to separated and impinging flows," in *Engineering turbulence modelling and experiments 5*. Editors W. Rodi, and N. Fueyo (Oxford: Elsevier Science Ltd), 107–116. doi:10.1016/B978-008044114-6/50009-0

Mangold, N. (2011). Ice sublimation as a geomorphic process: A planetary perspective. *Geomorphology* 126, 1–17. doi:10.1016/j.geomorph.2010.11.009

Massé, M., Bourgeois, O., Le Mouélic, S., Verpoorter, C., Le Deit, L., and Bibring, J. P. (2010). Martian polar and circum-polar sulfate-bearing deposits: Sublimation tills derived from the North Polar Cap. *Icarus* 209, 434–451. doi:10.1016/j.icarus.2010.04.017

Massé, M., Bourgeois, O., Mouélic, S. L., Verpoorter, C., Spiga, A., and Deit, L. L. (2012). Wide distribution and glacial origin of polar gypsum on Mars. *Earth Planet. Sci. Lett.* 317-318, 44–55. doi:10.1016/j.epsl.2011.11.035

McKinnon, W. B., Nimmo, F., Wong, T., Schenk, P. M., White, O. L., Roberts, J. H., et al. (2016). Convection in a volatile nitrogen-ice-rich layer drives Pluto's geological vigour. *Nature* 534, 82–85. doi:10.1038/nature18289

Meakin, P., and Jamtveit, B. (2010). Geological pattern formation by growth and dissolution in aqueous systems. *Proc. R. Soc. A Math. Phys. Eng. Sci.* 466, 659–694. doi:10.1098/rspa.2009.0189

Mellor, M., and Swithinbank, C. (1989). *Airfields on Antarctic glacier ice*. Hanover NH: Cold Region Research and Engineering Lab. Tech. rep.

Milanovic, P., Maksimovich, N., and Meshcheriakova, O. (2019). *Dams and reservoirs in evaporites*.

Milkovich, S. (2006). Surface textures of mars' north polar layered deposits: A framework for interpretation and future exploration. *Mars J.* 21, 21–45. doi:10.1555/mars.2006.0003

Millour, E., Forget, F., Spiga, A., Vals, M., Zakharov, V., Montabone, L., et al. (2018). "The mars climate Database (version 5.3)," in *Scientific workshop: "From Mars express to ExoMars" (ESAC madrid)*, 27–28.

Moore, J. M., Howard, A. D., Umurhan, O. M., White, O. L., Schenk, P. M., Beyer, R. A., et al. (2018). Bladed terrain on pluto: Possible origins and evolution. *Icarus* 300, 129–144. doi:10.1016/j.icarus.2017.08.031

Moore, J. M., Howard, A. D., Umurhan, O. M., White, O. L., Schenk, P. M., Beyer, R. A., et al. (2017). Sublimation as a landform-shaping process on Pluto. *Icarus* 287, 320–333. doi:10.1016/j.icarus.2016.08.025

Moores, J. E., Smith, C. L., Toigo, A. D., and Guzewich, S. D. (2017). Penitentes as the origin of the bladed terrain of tartarus dorsa on pluto. *Nature* 541, 188–190. doi:10.1038/nature20779

Morison, A., Labrosse, S., and Choblet, G. (2021). Sublimation-driven convection in sputnik planitia on pluto. *Nature* 600, 419–423. doi:10.1038/s41586-021-04095-w

Morse, J. W., and Arvidson, R. S. (2002). The dissolution kinetics of major sedimentary carbonate minerals. *Earth-Science Rev.* 58, 51–84. doi:10.1016/S0012-8252(01)00083-6

Ng, F. S., and Zuber, M. T. (2006). Patterning instability on the Mars polar ice caps. *J. Geophys. Res. E Planets* 111. doi:10.1029/2005JE002533

Nguyen, T. G., Radebaugh, J., Innanen, A., and Moores, J. E. (2020). A survey of small-scale (<50 m) surface features on the Martian north polar cap using HiRISE. *Planet. Space Sci.* 182, 104809. doi:10.1016/j.pss.2019.104809

Obleitner, F., and Spötl, C. (2011). The mass and energy balance of ice within the Eisriesenwelt cave, Austria. *Cryosphere* 5, 245–257. doi:10.5194/tc-5-245-2011

Ohmura, A. (2004). Cryosphere during the twentieth century. *Geophys. Monogr. Ser.* 150, 239–257. doi:10.1029/150GM19

Pankine, A. A., and Tamppari, L. K. (2015). Constraints on water vapor vertical distribution at the Phoenix landing site during summer from MGS TES day and night observations. *Icarus* 252, 107–120. doi:10.1016/j.icarus.2015.01.008

Pankine, A. A., Tamppari, L. K., and Smith, M. D. (2010). MGS TES observations of the water vapor above the seasonal and perennial ice caps during northern spring and summer. *Icarus* 210, 58–71. doi:10.1016/j.icarus.2010.06.043

Petrosyan, A., Galperin, B., Larsen, S. E., Lewis, S., Maattanen, A., Read, P. L., et al. (2011). The Martian atmospheric boundary layer. *Rev. Geophys.* 49. doi:10.1029/2010RG000351

Port, S. T., Chevrier, V. F., and Kohler, E. (2020). Investigation into the radar anomaly on Venus: The effect of Venus conditions on bismuth, tellurium, and sulfur mixtures. *Icarus* 336, 113432. doi:10.1016/j.icarus.2019.113432

Protopapa, S., Grundy, W. M., Reuter, D. C., Hamilton, D. P., Dalle Ore, C. M., Cook, J. C., et al. (2017). Pluto's global surface composition through pixel-by-pixel Hapke modeling of New Horizons Ralph/LEISA data. *Icarus* 287, 218–228. doi:10.1016/j.icarus.2016.11.028

Schaefer, L., and Fegley, F. (2004). Heavy metal frost on Venus. *Icarus* 168, 215–219. doi:10.1016/j.icarus.2003.11.023

Schenk, P. M. (1991). Fluid volcanism on Miranda and ariel: Flow morphology and composition. *J. Geophys. Res.* 96, 1887–1906. doi:10.1029/90jb01604

Schmitt, B., Philippe, S., Grundy, W. M., Reuter, D. C., Côte, R., Quirico, E., et al. (2017). Physical state and distribution of materials at the surface of Pluto from New Horizons LEISA imaging spectrometer. *Icarus* 287, 229–260. doi:10.1016/j.icarus.2016.12.025

Scully, J. E., Russell, C. T., Yin, A., Jaumann, R., Carey, E., Castillo-Rogez, J., et al. (2015). Geomorphological evidence for transient water flow on Vesta. *Earth Planet. Sci. Lett.* 411, 151–163. doi:10.1016/j.epsl.2014.12.004

Skorov, Y. V., Markiewicz, W. J., Basilevsky, A. T., and Keller, H. U. (2001). Stability of water ice under a porous nonvolatile layer: Implications to the south polar layered deposits of Mars. *Planet. Space Sci.* 49, 59–63. doi:10.1016/S0032-0633(00)00121-5

Smith, I. B., and Holt, J. W. (2010). Onset and migration of spiral troughs on Mars revealed by orbital radar. *Nature* 465, 450–453. doi:10.1038/nature09049

Smith, I. B., Holt, J. W., Spiga, A., Howard, A. D., and Parker, G. (2013). The Spiral troughs of Mars as cyclic steps. *J. Geophys. Res. Planets* 118, 1835–1857. doi:10.1002/jgre.20142

Smith, I. B., and Spiga, A. (2018). Seasonal variability in winds in the north polar region of Mars. *Icarus* 308, 188–196. doi:10.1016/j.icarus.2017.10.005

Sori, M. M., Bapst, J., Becerra, P., and Byrne, S. (2019). Islands of ice on mars and pluto. *J. Geophys. Res. Planets* 124, 2522–2542. doi:10.1029/2018JE005861

Strobel, D. F., and Zhu, X. (2017). Comparative planetary nitrogen atmospheres: Density and thermal structures of Pluto and Triton. *Icarus* 291, 55–64. doi:10.1016/j.icarus.2017.03.013

Stubbs, T. J., and Wang, Y. (2012). Illumination conditions at the Asteroid 4 Vesta: Implications for the presence of water ice. *Icarus* 217, 272–276. doi:10.1016/j.icarus.2011.11.007

Telfer, M. W., Parteli, E. J. R., Radebaugh, J., Beyer, R. A., Bertrand, T., Forget, F., et al. (2018). Dunes on pluto. *Science* 360, 992–997. doi:10.1126/SCIENCE.AAO2975

Thomas, R. (1979). Size of scallops and ripples formed by flowing water. *Nature* 277, 281–283. doi:10.1038/277281a0

Thorness, C. B., and Hanratty, T. J. (1979). Mass transfer between a flowing fluid and a solid wavy surface. *AIChE J.* 25, 686–697. doi:10.1002/aic.690250415

Trowbridge, A. J., Melosh, H. J., Steckloff, J. K., and Freed, A. M. (2016). Vigorous convection as the explanation for Pluto's polygonal terrain. *Nature* 534, 79–81. doi:10.1038/nature18016

van den Broeke, M. R., and Bintanja, R. (1995). Ummertime atmospheric circulation in the vicinity of a blue ice area in Queen Maud Land, Antarctica. *Boundary-Layer Meteorol.* 72, 411–438. doi:10.1007/BF00709002

Weller, G. (1969). The heat and mass balance of snow dunes on the central Antarctic plateau. *J. Glaciol.* 8, 277–284. doi:10.3189/S0022143000031257

White, O. L., Moore, J. M., McKinnon, W. B., Spencer, J. R., Howard, A. D., Schenk, P. M., et al. (2017). Geological mapping of sputnik planitia on pluto. *Icarus* 287, 261–286. doi:10.1016/j.icarus.2017.01.011

Winkler, M., Juen, I., Mölg, T., Wagnon, P., Gómez, J., Kaser, G., et al. (2009). Measured and modelled sublimation on the tropical glaciar artesonraju, perú. *Cryosphere* 3, 21–30. doi:10.5194/tc-3-21-2009